

RESEARCH ARTICLE OPEN ACCESS

A Computational Study of the Oxidation of the Phenanthryl Radical $C_{14}H_9\cdot$: Thermochemistry and Possible Reaction Pathways

Nadia Sebbar | Henning Bockhorn | Dimosthenis Trimis

KIT- Karlsruhe Institute of Technology, Engler-Bunte-Institut, Verbrennungstechnik, Karlsruhe, Germany

Correspondence: Nadia Sebbar (nadia.sebbar@partner.kit.edu)

Received: 20 January 2025 | **Revised:** 28 July 2025 | **Accepted:** 24 November 2025

ABSTRACT

In this computational study, the reaction of the phenanthryl radical $C_{14}H_9\cdot$ ($A_3\cdot$) with molecular and atomic oxygen as part of the reaction mechanism of the oxidation of phenanthrene is investigated. Pathways resulting from the $A_3\cdot + {}^3O_2$ and $A_3\cdot + O$ reaction systems are examined using DFT quantum chemistry calculations. The energetics of the involved intermediates, products, and transition state structures are determined, as well as the kinetics of possible reaction pathways. Similar to the oxidation of smaller systems ($A_1\cdot$ (phenyl) or $A_2\cdot$ (naphthyl)), the addition of 3O_2 to the phenanthryl radical $A_3\cdot$ results in a peroxy radical $C_{14}H_9OO\cdot$ ($A_3OO\cdot$) with some 50 kcal mol⁻¹ of energy released, allowing further propagation and/or chain branching reactions. Standard enthalpies of formation as well as entropies and heat capacities are calculated using DFT methods (B3LYP, M06, APFD). Similar to the oxidation of the naphthyl radical, six primary subsequent pathways for the stabilized peroxy $A_3OO\cdot$ are investigated with barriers below the energy of the starting point $A_3\cdot + {}^3O_2$. The reaction channels were investigated down to the next smaller PAH-radical (naphthyl $A_2\cdot$) and the corresponding reaction products. Important exothermic chain branching reactions are taking place, and several unsaturated oxygenated hydrocarbon intermediates are identified and determined. For the identified pathways, kinetic parameters based on canonical transition state theory (CTST) are calculated and reported in this study.

1 | Introduction

One measure for reducing the emission of particulate matter (PM) from vehicles driven by diesel or gasoline-fueled internal combustion engines is the application of particulate filters (PF). In operation, PFs are trapping soot particles present in the exhaust gases and ideally are continuously regenerated by oxidation of the deposited soot with residual oxygen at temperatures in the range of about 400°C to 600°C, and approximately ambient pressure. Oxygen may be considered the essential molecule activating the oxidation. Soot oxidation kinetics and the knowledge of soot oxidation mechanisms, therefore, are crucial for the regeneration of PFs and the control of PM emissions.

Soot from internal combustion engines consists of aggregates of sub- μ primary particles, to a large extent composed of stacked graphene-like layers [1] for which large polycyclic aromatic hydrocarbons (PAHs) can serve as approximate models. Then, the oxidation of PAHs under conditions prevailing in the exhaust gas of internal combustion engines may serve as a starting point for developing oxidation mechanisms and oxidation kinetics of soot primary particles.

In previous work [2–4], the oxidation of a series of PAHs, A_x with $2 \leq x \leq 7$, has been investigated. In Ref. [2], the first reaction steps of the oxidation of PAHs by molecular oxygen have been studied. It turned out that the primary attack of O_2 on A_x , A_x

This is an open access article under the terms of the [Creative Commons Attribution](https://creativecommons.org/licenses/by/4.0/) License, which permits use, distribution and reproduction in any medium, provided the original work is properly cited.

© 2025 The Author(s). *International Journal of Chemical Kinetics* published by Wiley Periodicals LLC.

+ O₂ → A_x• + HOO•, is quite similar for the different PAHs. Also, the addition of O₂ to the radical A_x•, forming a peroxy radical, A_x• + O₂ → A_xO₂•, reveals similarities. At temperatures of about 1000 K, the most dominant subsequent reaction step is the ipso addition of the terminal oxygen of the peroxy group to the same carbon atom group through formation of a three-membered COO ring at the edge of A_x•Y(COO) radicals. Reaction pathways resulting from possible subsequent reactions of these peroxides, as well as the associated energy barriers, are identified and reported in [2]. Detailed results concerning A₁ and the oxidation of A₁• via various intermediate species to the final products C₂H₂, CO, and CO₂ are reported in ref. [3]. Likewise, the oxidation of A₂• has been investigated in detail in ref. [4]. The principal result from this study is that the consecutive reactions of the A₂• radical, viz. the channels conducting to a phenyl radical C₆H₅• and CO, CO₂, and C₂H₂, are by orders of magnitude faster than the activation of naphthalene by oxygen (A₂ + O₂ → A₂• + HOO•). This supports the hypothesis that the pathways producing CO, C₆H₅•, and C₂H₂ may constitute a repetitive reaction sequence for the successive diminution of six-membered rings also in larger polycyclic aromatic hydrocarbons. To support and expand this hypothesis, this work continues the series of PAHs with phenanthrene (A₃), containing three aromatic rings, and the oxidation of the phenanthryl radical A₃•. This approach is also based on literature data showing that the oxidation of the pyrenyl radical A₄• leads to the phenanthryl radical A₃• [5, 6], partly verifying the above hypothesis. The study investigates the attack of molecular oxygen on the phenanthryl radical A₃• and possible reactions following the primary attack. Structures, thermochemical properties, and reaction kinetics of the involved species are estimated. The objective is to employ small aromatic hydrocarbons as model molecules for higher polycyclic aromatic hydrocarbons and to develop mechanisms and reaction kinetics for the oxidation of the graphene layers within soot primary particles.

Due to their armchair structures, phenanthryl radicals favor the oxidation [7]. Several studies have reported experimental and numerical investigations on the oxidation of phenanthrene. In the study of Barbas et al. [8] on the photochemical oxidation of phenanthrene adsorbed on silica gel in the presence of air, several products have been identified issuing from the addition of the singlet molecular oxygen to the ground state of phenanthrene with subsequent thermal and/or photochemical reactions of the initially formed product. Yang and Hildebrand [9] have studied the degradation and oxidation of phenanthrene in subcritical water discerning that the stability of phenanthrene in water was quite poor at the presence of dissolved oxygen, especially at temperatures higher than 150°C. Based on gas chromatography/mass spectrometry (GC/MS) results, they reported that most of the phenanthrene degradation products are oxygen-containing aromatic compounds (e.g., phenol, benzoic acid, and ketones), indicating that the dissolved oxygen was responsible for phenanthrene degradation in subcritical water. Perraudin et al. [10] investigated primary products of the reaction of gas-phase ozone with anthracene and phenanthrene adsorbed on silica model particles. The adopted kinetic approach identified anthraquinone, anthrone, and 1,1'-biphenyl-2,2'-dicarboxaldehyde as the primary products of the oxidation reactions. The reaction of gaseous phenanthrene with OH radicals in the presence of NO_x has been investigated by Lee and Lane [11]. Several oxidation products were

identified, such as 9-fluorenone, 1,2-naphthalic anhydride, 2,2'-diformylbiphenyl, dibenzopyranone, phenanthrols, nitrophenanthrenes, 1,4-phenanthrenequinone, 9,10-phenanthrenequinone, and nitrodibenzopyranones.

In their computational study, Edwards et al. [7] determined the energetics and kinetics of the thermal decomposition of oxyradicals bonded to a graphene armchair edge. Among others, phenanthrene was selected as a substrate to model the armchair edge. For a given arbitrarily shaped PAH, oxidation should preferentially occur at armchair and corner zigzag sites, leaving inner zigzag sites resistant to oxidation essentially intact. Edwards et al. [12] investigated computationally the oxidation of phenanthrene by hydroxyl radicals using density functional theory (DFT) methods. They worked out that, in contrast to A₁ + OH and A₁/C₆H₅OH + OH, A₃• + OH leads to multiple pathways for the formation of CO. The oxidation of phenanthryl radicals by OH is governed by H atom migration/elimination and oxyradical decomposition due to a possible rearrangement of the aromatic edge with favorable decomposition rates. Zhao et al. [13] investigated OH radical-initiated degradation of phenanthrene in the presence of O₂ and NO_x at atmospheric conditions. They elucidated possible reaction mechanisms by DFT calculations, with the result that the main products are a series of oxygenated PAHs with retained or opened aromatic rings containing phenanthrol, phenanthrones, phenanthrenequinone, and dialdehydes. Maranzana et al. [14] studied the NO₃-initiated gas phase oxidation of anthracene and phenanthrene in the presence of O₂, NO, and NO₂ with the help of DFT methods to show the mechanistic features of the NO₃-initiated oxidative degradation.

The formation of phenanthrene via recombination of indenyl (C₉H₇) and cyclopentadienyl (C₅H₅) radicals has been investigated with quantum chemistry G3-(MP2, CC)//B2PLYPD3/6-311G(d, p) methods in [15]. As the primary products of the reaction C₉H₇ + C₅H₅ → C₁₄H₁₁ + H, benzofulvalene has been identified, most favorable in terms of the entropy factor and hence preferable at higher temperatures, or after significant structural rearrangements, phenanthrene, anthracene, or benzoazulenes. Using DFT and composite methods (B3LYP, M062X, and CBS-QB3), Fikri and Raj [16] developed a detailed reaction mechanism for the conversion of acenaphthylene to phenanthrene comprising two pathways. They report that the reactions in both pathways progress via the formation of two fused five-membered rings and H-migration with subsequent conversion to a six-membered ring and the formation of either phenanthrene or the phenanthryl radical.

In the present work, the reaction of the phenanthryl radical C₁₄H₉• (A₃•) with molecular and atomic oxygen as part of the oxidation reactions of phenanthrene down to the species C₁₀H₇•, CO, and C₂H₂ is examined using DFT quantum chemistry calculations. The calculations were performed employing different computational methods, viz. B3LYP, M06, as well as APFD. Enthalpies of formation of the species as well as transition state structures involved in the investigated reaction systems A₃• + O₂ / A₃• + O are calculated. The kinetic parameters of each path are determined using chemical activation analysis based on canonical transition state theory (CTST) calculations. The reaction rate coefficients help to identify the importance of the different reaction paths for the different reactions.

2 | Computational Methods

2.1 | Quantum Chemistry Calculations—Density Functional Methods

Using the Gaussian 16 program suite [17, 18], the molecular properties of the species (intermediates, transition state structures, and products) resulting from the oxidation of phenanthrene (A_3) and the phenanthryl radical ($A_3\cdot$) are calculated. For the computations, DFT methods, viz. M06 [19, 20], the newly developed APFD [21], and the B3LYP [22–24] are used. In a previous study [4], the oxidation of a two-ring system (naphthyl) has been considered as part of a series of calculations in which the number of rings will be increased gradually towards larger polycyclic aromatic hydrocarbons. The use of DFT methods suggested here is affordable and permits handling large molecules.

2.2 | Thermodynamic Properties and Kinetic Parameters

The standard enthalpy of formation of the species involved in the system (radicals, stable molecules, and transition state structures) is calculated with the help of isodesmic reactions whenever possible. The use of working reactions with similar bonding environments near each atom on both sides of the equations leads to cancellation of errors and further increases the accuracy. Isodesmic reactions combine the unknown formation enthalpy of the considered species with experimental or previously evaluated enthalpies of formation needed in the isodesmic analysis. The transition state structures are identified by their single imaginary frequency, whose vibration mode moves between the reactant and the product.

The calculated enthalpies of formation along with the energy barriers resulting from B3LYP, M06, and APFD are reported in Supporting Information 1 for comparison. As is obvious from the tables in Supporting Information 1, the values resulting from the three methods are reproducible and very close together, and the finally selected values can therefore be considered validated. For further calculations, the results from APFD, which is considered the newest and most accurate method, are mostly selected. Generally, the selection is based on the calculated geometry after visualizing with the GaussView module from Gaussian 16.

Entropy and heat capacity calculations are based on the vibration frequencies and moments of inertia obtained from the optimized APFD/6-311G(d,p) structures (DFT calculations). The SMCPS code [25], based on formulas from statistical mechanics, does not consider torsional frequencies. Instead, hindered internal rotor contributions to entropy and heat capacities are determined in this work at B3LYP/6-31G(d,p) using the ROTATOR program [26]. Enthalpies of formation $\Delta H_{f,298}^0$, entropies S_{298}^0 and heat capacities $C_p(T)$ are calculated for all species (adduct, intermediates, products, and transition state structures) involved in the investigated system $A_3/A_3\cdot + O_2/O$. The structure of each compound is illustrated in Table A1. The thermodynamic properties are converted into the NASA polynomial format using the THERMFIT code [25]. Values of enthalpies of formation $\Delta H_{f,298}^0$, entropies S_{298}^0 and heat capacities $C_p(T)$ and the corresponding conversion to

the NASA polynomials, including geometries, frequencies, and moment of inertia, are listed in Supporting Information 2.

With the help of ThermKin [25], the forward rate coefficients, $k(T)$, based on the canonical transition state theory (CTST), are determined. Entropy differences between the reactants and transition states are used to determine the pre-exponential factors A via CTST. The modified Arrhenius parameters are determined from least squares regression analysis. In addition, multi-channel, multi-frequency QRRK calculations are performed for $k(E)$ with master equation analysis (CHEMASTER code [27]) for the primary subsequent reaction steps following the addition of $A_3\cdot + {}^3O_2$ to calculate fall-off and pressure and temperature dependence of the reaction rate coefficients. From this kinetic analysis, fall-off and pressure-dependent rate coefficients for the primary subsequent reactions are obtained from the calculated energies, vibration frequencies, and structures, and important reaction pathways are identified.

3 | Results and Discussion

3.1 | Formation of Phenanthryl Radicals

The H-abstraction from phenanthrene (A_3) by oxygen, $C_{14}H_{10} + {}^3O_2 \rightarrow C_{14}H_9\cdot + HOO\cdot$ can take place at five different carbon sites, resulting in five radical isomers, $C_{14}H_9\cdot$ ($A_3\cdot$), as illustrated in Table 1. The energies required for the H-abstraction from these different sites of the stable phenanthrene are listed in Table 1. The energy for the abstraction of a hydrogen by molecular oxygen is approximately independent of the position of the carbon site. The energy barriers for the abstraction from the different sites amount to ca. 66 kcal mol^{−1} relative to the stable phenanthrene molecule (A_3). The five corresponding radicals lie at the same level of energy at about 109 kcal mol^{−1}, which is in good agreement with the values reported by Wang and Frenklach [28]. For this study, the radical in “E” position is chosen for further investigation because it is a direct product of the pyrenyl radical oxidation [5, 6].

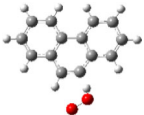
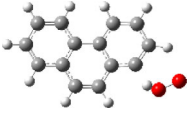
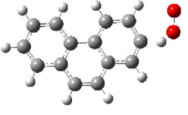
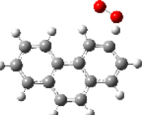
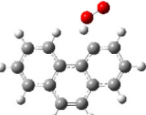

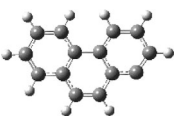

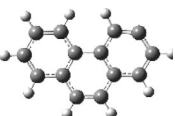
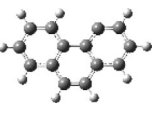
Figure 1 illustrates the major channels for the reaction $A_3\cdot + O_2$. The reaction pathways are similar to the previously investigated systems A_1 [2, 3] and A_2 [2, 4], and for a better comparison, the same scheme is used. Several pathways lead to the formation of the naphthyl radical $A_2\cdot$ and CO and C_2H_2 . Detailed consideration and discussion of each channel is presented in the following sections.

3.2 | Reactions of the Phenanthryl Radical $A_3\cdot$ ($C_{14}H_9\cdot$) With O_2

3.2.1 | Formation of a Stable Peroxy Radical $A_3OO\cdot$ (Channel 1)

Similar to other systems [4, 30, 31], the addition of molecular oxygen to the phenanthryl radical $A_3\cdot$ proceeds without barrier and with an excess of energy due to the formation of the intermediate peroxy radical $A_3OO\cdot$. Due to the armchair structure, the energy released during the peroxy formation with 45.6 kcal mol^{−1} is some 4 kcal mol^{−1} lower than that released during the formation of the two-ring peroxy radical $A_2OO\cdot$ as discussed in Ref. [2]. The

TABLE 1 | Energy barriers for the formation of $A_3\cdot$ ($C_{14}H_9\cdot$) isomers through H-abstraction by O_2 . Comparison of results calculated with the applied methods; values obtained with APFD/6-311G(d,p) are written in bold face.

$C_{14}H_{10} + {}^3O_2 \rightarrow TS-A_3\cdot \rightarrow C_{14}H_9\cdot + HOO\cdot$ Phenanthrene (A_3) $\Delta H_{f298}^0 = 48.33 \text{ kcal mol}^{-1}$ [29]					
ΔH_{f298}^0 (kcal mol $^{-1}$)	TS- $A_3\cdot$ -A	TS- $A_3\cdot$ -B	TS- $A_3\cdot$ -C	TS- $A_3\cdot$ -D	TS- $A_3\cdot$ -E
					
B3LYP/ 6-311G(d,p)	116.9	118.7	118.3	117.51	117.1
M06/ 6-311G(d,p)	114.0	114.9	115.4	113.8	113.1
APFD/ 6-311G(d,p)	115.2	115.9	116.7	114.8	114.2
	$A_3\cdot$ -A	$A_3\cdot$ -B	$A_3\cdot$ -C	$A_3\cdot$ -D	$A_3\cdot$ -E
					
B3LYP/ 6-311G(d,p)	109.9	111.8	110.0	111.6	109.8
M06/ 6-311G(d,p)	110.0	110.3	109.6	109.6	108.1
APFD/ 6-311G(d,p)	110.4	110.2	110.2	109.6	108.3

available energy favors consecutive reactions of the chemically activated phenanthryl-peroxy radical $[A_3OO\cdot]^\#$, six of which are illustrated in Figure 2.

Channel 1.1: Addition of the oxygen radical to the adjacent carbon atom of the same ring via **TS1.1-1**.

Channel 1.2: Ipso addition of the oxygen radical via **TS1.2-1**.

Channel 1.3: Addition of the oxygen atom to the carbon of the opposite ring via **TS1.3-1**.

Channel 1.4a: Hydrogen abstraction by the oxygen atom from the carbon of the same six-membered ring via **TS1.4a-1**.

Channel 1.4b: Hydrogen abstraction by the oxygen from the carbon of the next six-membered ring via **TS1.4b-1**.

Channel 2: RO—O bond cleavage via **TS2-1**.

All barriers lie below the energy of $A_3\cdot + O_2$.

3.2.2 | Formation of $A_3\cdot YC_2O_2$ Through Addition of the Oxygen Atom to the Adjacent Carbon Atom (Channel 1.1)

Similar to the two-ring system investigated in previous work [4], one of the subsequent reactions of the peroxy radical $A_3OO\cdot$ is the addition of the radical oxygen to the adjacent carbon of the same ring via **TS1.1-1** (see Figure 3). The energy required for the opening of the C=C double bond is ca. 37 kcal mol $^{-1}$ relative to

the peroxy $A_3OO\cdot$ radical. This is some 7 kcal mol $^{-1}$ less compared with the energy required for the two-membered ring ($A_2OO\cdot$) [4]. The weak O—O bond in the radical $A_3\cdot YC_2O_2$ (101.6 kcal mol $^{-1}$) is opened with the release of 67.5 kcal mol $^{-1}$ forming ortho- $A_3O\cdot DO$ at 34.1 kcal mol $^{-1}$. Two paths are possible for the subsequent reactions of the oxygen radical site of ortho- $A_3O\cdot DO$.

The first path occurs through **TS1.1-3**, attaching the oxygen radical to the carbonyl carbon through a small barrier of 8.8 kcal mol $^{-1}$, forming a seven-membered ring $A_2YCDOOC\cdot CC$ at 12.8 kcal mol $^{-1}$. The further reaction path of this species unites with Channel 1.2A and is discussed in Section 3.2.3, see Figure 4.

The second path illustrated in Figure 3 proceeds through addition of the oxygen to the adjacent non-carbonyl carbon via **TS1.1-4** over a low barrier of 4 kcal mol $^{-1}$ to form a three-membered ring $A_3\cdot DOYC_2O$ lying at ca. 29 kcal mol $^{-1}$. The latter radical rearranges over 5 kcal mol $^{-1}$ (**TS1.1-5**) and opens the three-membered ring to a radical with a seven-membered ring $A_2YC_2OC\cdot CDO$ at 34 kcal mol $^{-1}$. The available energy released during ortho- $A_3O\cdot DO$ formation allows the opening of the seven-membered ring over 38.3 kcal mol $^{-1}$ (**TS1.1-6**), resulting in the $A_2CC\cdot CDOCDO$ radical at 54.8 kcal mol $^{-1}$, which undergoes successive dissociation reactions. A C_2H_2 elimination reaction takes place via **TS1.1-7** through a ca. 40 kcal mol $^{-1}$ energy barrier to form $A_2\cdot CDOCDO$ followed by an intramolecular hydrogen abstraction via only 3 kcal mol $^{-1}$ (**TS1.1-8**) to $A_2CDOC\cdot DO$ lying 24 kcal mol $^{-1}$ lower in energy. Two successive CO eliminations

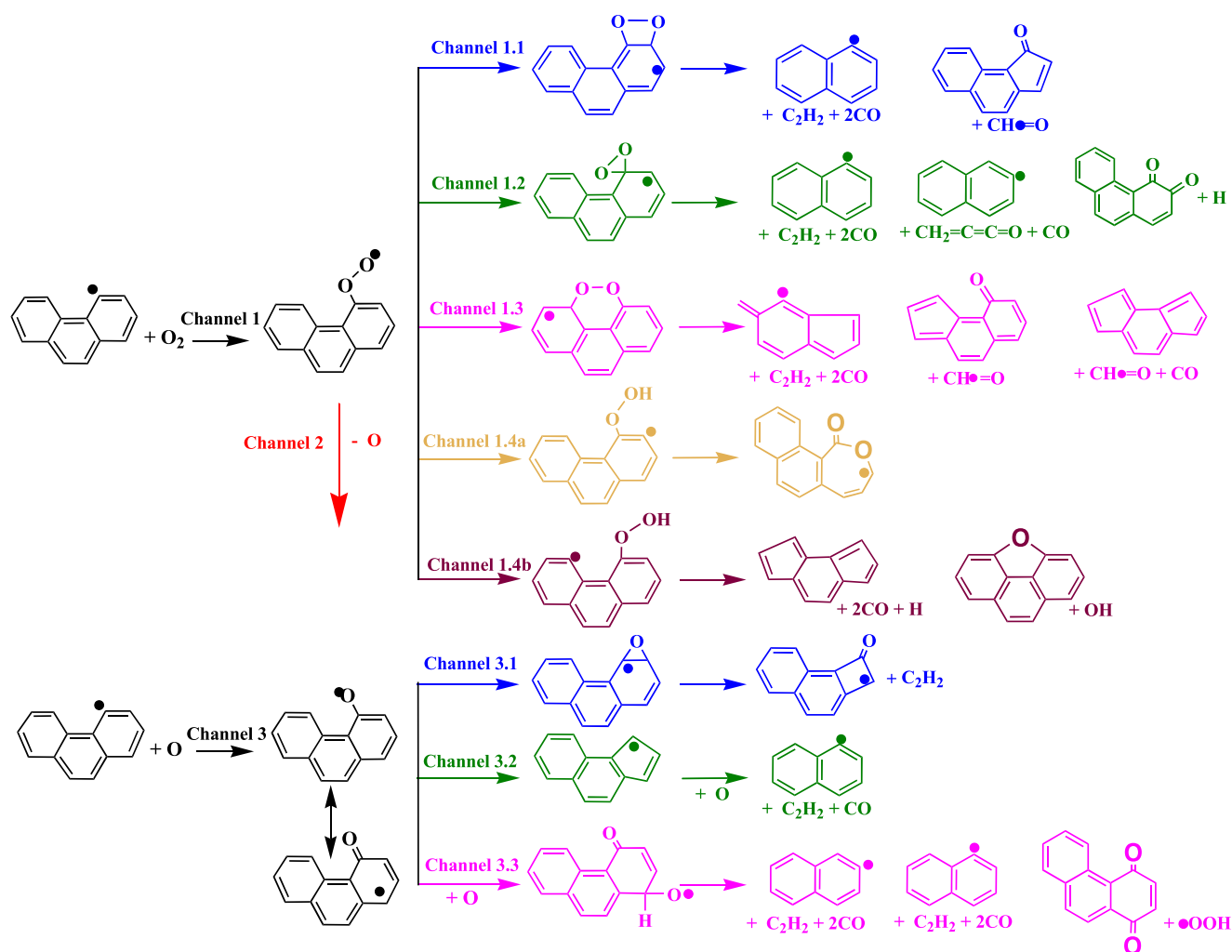


FIGURE 1 | Major reaction channels for $A_3\bullet + O_2$ and $A_3\bullet + O$.

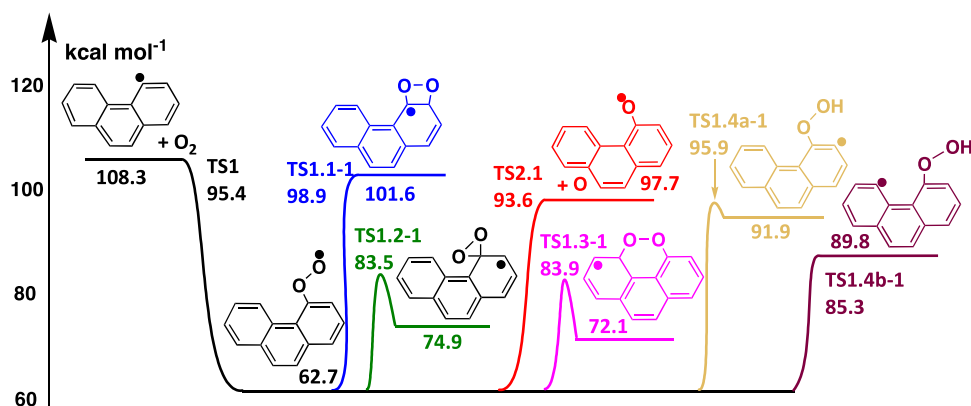


FIGURE 2 | Potential diagram for primary consecutive reaction channels for $A_3OO\bullet$.

then take place via **TS1.1-9** and **TS1.1-10** to the 1-naphthyl radical. The alternative path of the $A_2CC\bullet CDOCD O$ radical is a barrierless $CH\equiv O$ elimination (**TS1.1-11**) followed by a five-membered ring closure to the stable A_2YC_5DO .

Alternatively, the $A_2YC_2OC\bullet CDO$ radical has the possibility for ring closure over ca. 34 kcal mol⁻¹ (**TS1.1-12**) to a fused bicycle $A_2YC_5DOYC_3\bullet O$ at 40.1 kcal mol⁻¹, followed by a low energy barrier C—O bond dissociation (**TS1.1-13**) resulting in

$A_2YC_5\bullet DOCD O$ at 10.2 kcal mol⁻¹. This last radical eliminates $CH\equiv O$ resulting in the stable A_2YC_5DO .

3.2.3 | Formation of $A_3\bullet YCO_2$ Through Ipso Addition of the Oxygen Atom to the Ring (Channel 1.2)

Figure 4 illustrates the addition of the terminal oxygen of the peroxy radical to the same carbon atom (ipso addition, Channel

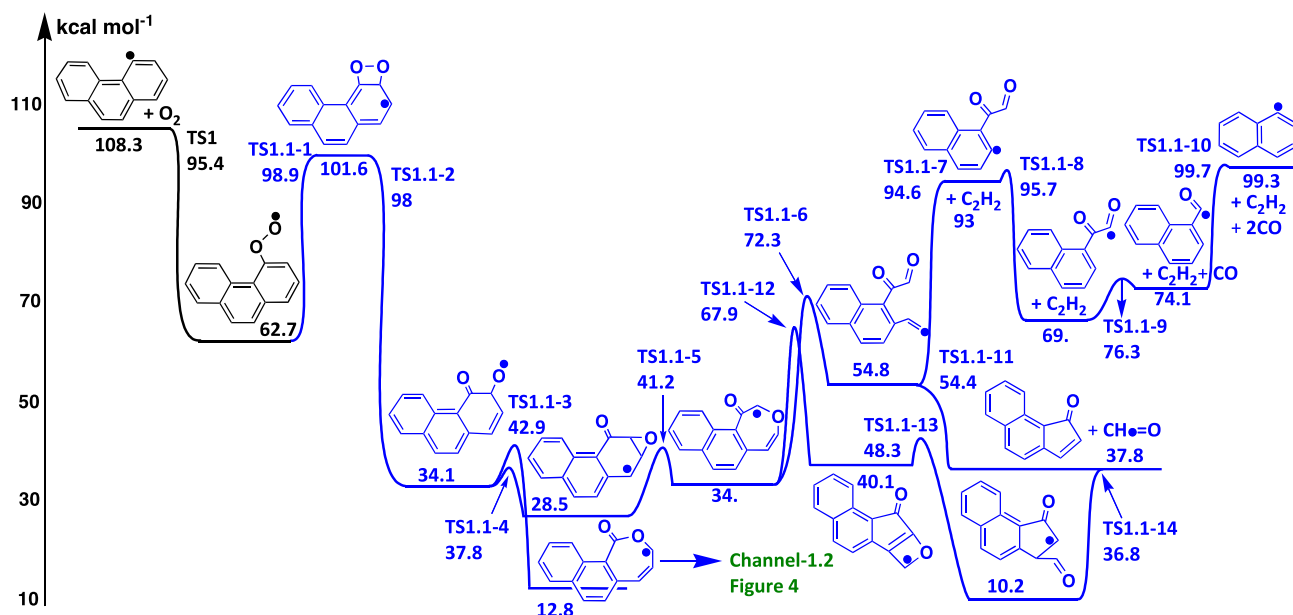


FIGURE 3 | Formation and further reactions of $A_3 \bullet YC_2O_2$ (Channel 1.1).

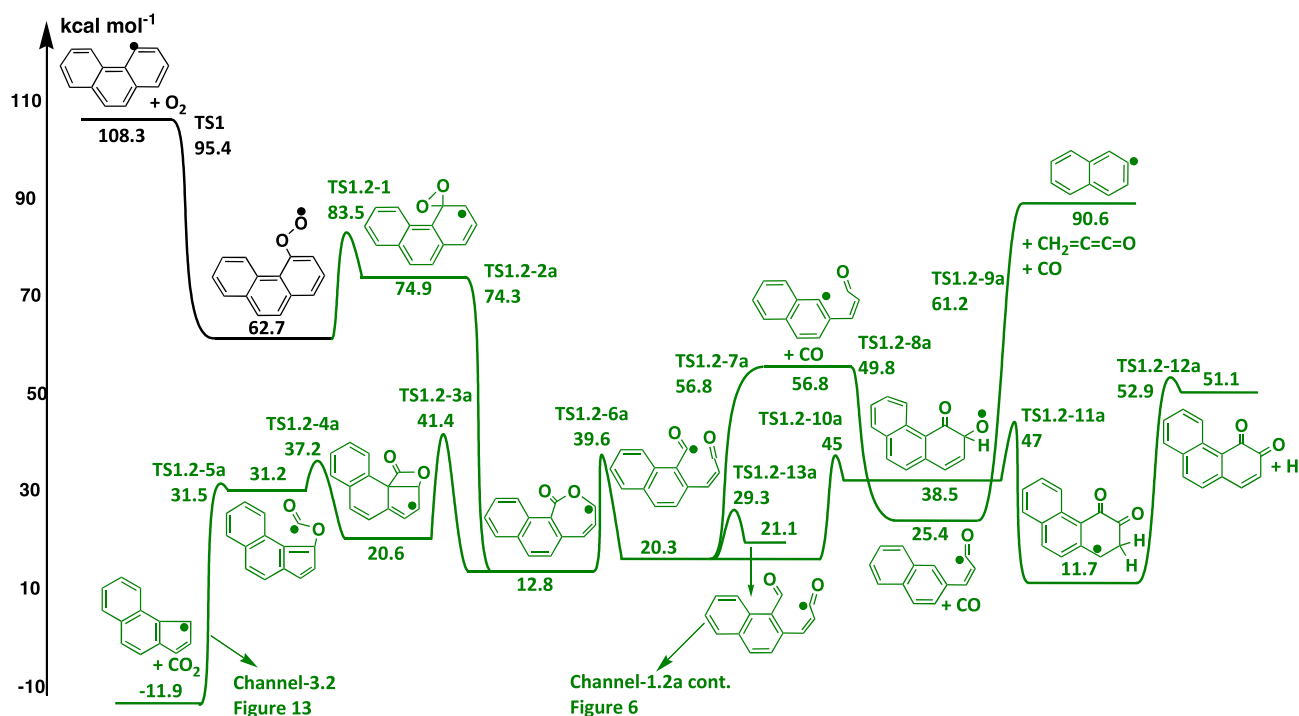


FIGURE 4 | Formation and further reactions of $A_3 \bullet YCO_2$ (Channel 1.2A).

1.2). This addition occurs over **TS1.2-1** and an energy barrier of ~ 21 kcal mol $^{-1}$ above the stabilized peroxide and formation of the three-membered ring peroxy radical $A_3 \bullet YCO_2$. As discussed in ref. [2], channel to $A_3 \bullet YCO_2$ formation is similar to that of the corresponding channel in a two-ring system. The energy of $A_3 \bullet YCO_2$ is calculated to be 74.9 kcal mol $^{-1}$, which is ca. 33 kcal mol $^{-1}$ below the energy at the starting point $A_3 \bullet + O_2$ of the channel, see Figures 4 and 6.

The weak O—O bond in the strained three-membered ring of the $A_3 \bullet YCO_2$ radical breaks, forming an immediate C=O double

bond to one oxygen and linking the other oxygen atom to the closest carbon atom at the right via Channel 1.2A (Figure 4) or at the left via Channel 1.2B (Figure 6).

Figure 4 illustrates Channel 1.2A in which the oxygen radical links to the adjacent carbon located on the right (**TS1.2-2a**), resulting in the formation of a lower energy radical $A_2YCDOOC \bullet CC$ at 12.8 kcal mol $^{-1}$. Another input to this channel at this point comes from Channel 1.1, see Figure 3. The energy of 61.5 kcal mol $^{-1}$ released during the formation of $A_2YCDOOC \bullet CC$ allows a C—C bond formation (**TS1.2-3a**) inside

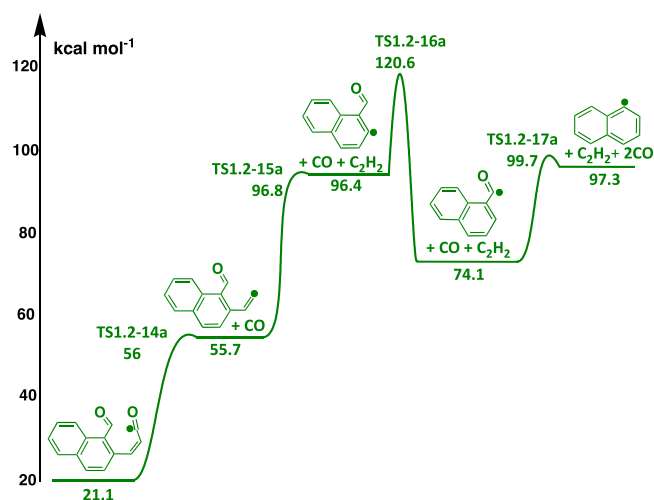


FIGURE 5 | Formation and further reactions of $A_3\bullet YCO_2$ (Channel 1.2A continuation).

the seven-membered ring, resulting in a four-membered ring $A_2YC_5\bullet YC_3ODO$ at 20.6 kcal mol⁻¹. This species opens one ring over some 17 kcal mol⁻¹ (via **TS1.2-4a**), resulting in $OC\bullet OYC_5A_2$ at 31.2 kcal mol⁻¹. This last intermediate dissociates easily (**TS1.2-5a**) to CO_2 and indenyl $A_2YC_5\bullet$, which subsequently is converted in Channel 3.2, see Figures 11 and 12.

Alternatively, $A_2YCD OOC\bullet CC$ can undergo a C—O bond scission over 27 kcal mol⁻¹ (**TS1.2-6a**) to form the $A_2C_3OC\bullet DO$ intermediate at 20.3 kcal mol⁻¹. Three channels are available for subsequent reactions of $A_2C_3OC\bullet DO$. One channel leads through a series of dissociation reactions, first removing one CO (**TS1.2-7a**) over some 36 kcal mol⁻¹ relative to $A_2C_3OC\bullet DO$ and forming $A_2\bullet C_3DO$. Via an exothermic intra-molecular hydrogen

shift (**TS1.2-8a**), a more stable compound $A_2C_2C\bullet DO$ is formed, releasing an excess of energy of 31.4 kcal mol⁻¹. This allows a second elimination (**TS1.2-9a**) to the stable $CH_2=C=C=O$ (CDCDCDO) + beta-naphthyl ($A_2\bullet$) via some 36 kcal mol⁻¹. The second channel for $A_2C_3OC\bullet DO$ starts with a new ring closure by forming a C—C bond via a barrier of ca. 25 kcal mol⁻¹ (**TS1.2-10a**) to $A_2ODA_1O\bullet$, which is followed by a shift of hydrogen (**TS1.2-11a**) over only 8.5 kcal mol⁻¹ to an intermediate $A_3\bullet DODO$ at a lower energy of 11.7 kcal mol⁻¹. Eliminating a hydrogen atom (**TS1.2-12a**) from the latter species leads to the stable 3,4-phenanthrenedione A_3DODO . The third path for $A_2C_3OC\bullet DO$ is an internal H-shift via a barrier of 9 kcal mol⁻¹ (**TS1.2-13a**) to $A_2CDOC_3\bullet O$ formed at 21.1 kcal mol⁻¹.

Figure 5 illustrates the subsequent dissociation reactions of $A_2CDOC_3\bullet O$ by CO elimination (**TS1.2-14a**) over some 35 kcal mol⁻¹ followed by the elimination of C_2H_2 (**TS1.2-15a**) via a barrier of 41 kcal mol⁻¹ to $A_2\bullet CDO$. The latter undergoes an H-transfer to form a more stable radical alpha- $A_2C\bullet DO$ (via **TS1.2-16a** and 24 kcal mol⁻¹), followed by a second CO elimination (**TS1.2-17a**) over ca. 25.2 kcal mol⁻¹ to the final products alpha- $A_2\bullet$ + CO.

In an alternative path, the oxygen can link to the closest carbon on the left after O—O bond scission in the three-membered ring of the $A_3\bullet YCO_2$ radical as illustrated in Figure 6 (Channel 1.2B). This reaction takes place over only 5 kcal mol⁻¹ (**TS1.2-2b**), releasing 69 kcal mol⁻¹ and forming $A_2YOCDOC\bullet CC$ at 6.0 kcal mol⁻¹. The first consecutive path available to the latter intermediate is via ring opening of $A_2YOCDOC\bullet CC$ (**TS1.2-3b**) over 28 kcal mol⁻¹, followed by a ring closure (**TS1.2-4b**) through 29 kcal mol⁻¹ to form $OC\bullet YC_5A_2$ at 28.9 kcal mol⁻¹. The latter radical loses barrierless one CO (**TS1.2-5b**) to $A_2YC_5\bullet O$, which forms a C—C bond (**TS1.2-6b**) to a five-membered ring $A_2YC_5O\bullet$. This last radical re-opens to $A_2\bullet C_3DO$ (via **TS1.2-7b**). A further

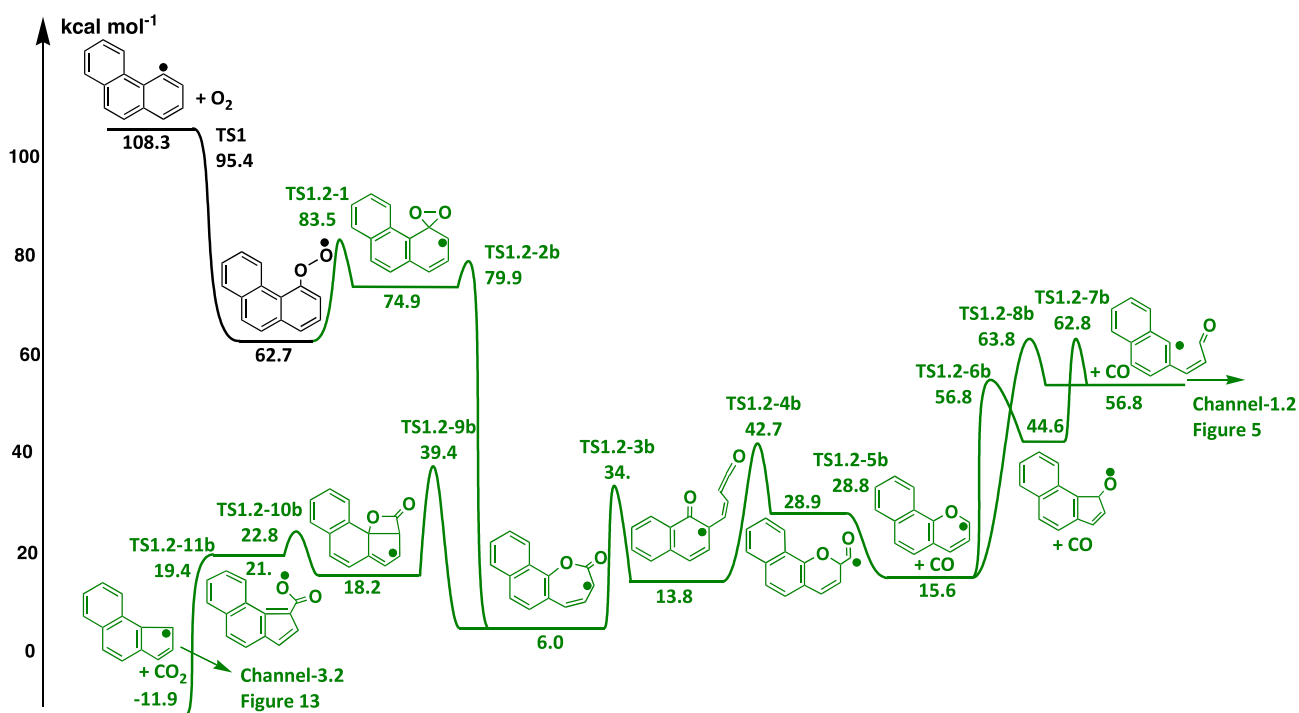


FIGURE 6 | Formation and further reactions of $A_3\bullet YCO_2$ (channel-1.2B).

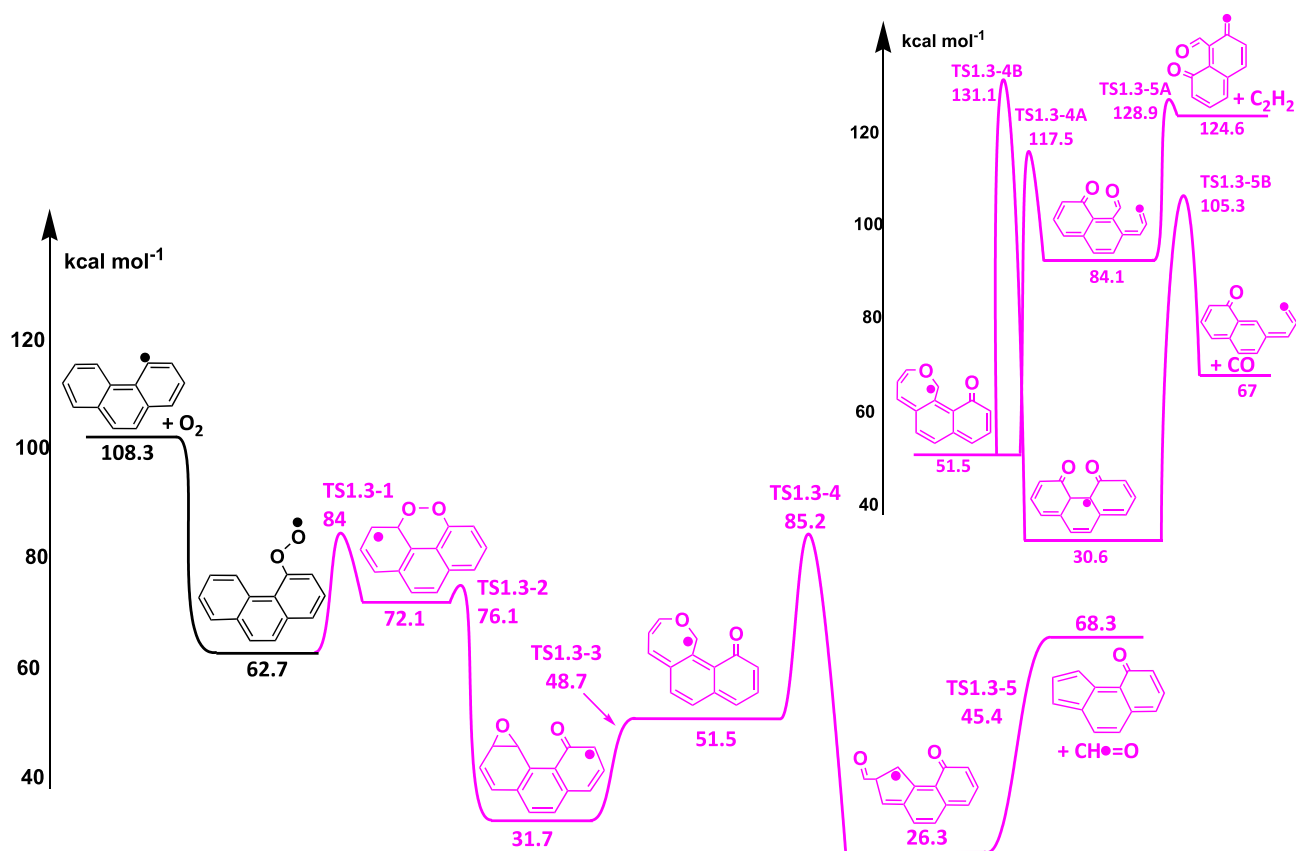


FIGURE 7 | Formation and further reactions of $A_3\bullet YC_4O_2$ (channel 1.3). The reactions displayed in the excerpt are not considered in this study.

alternative to $A_2YC_5\bullet O$ is the direct C—O bond scission (**TS1.2-8b**) to $A_2\bullet C_3DO$. Subsequent reactions of $A_2\bullet C_3DO$ occur in Channel 1.2, see Figure 4.

Compared to Channel 1.2A, the seven-membered ring of $A_2YOCDOC\bullet CC$ can close an internal C—C bond (**TS1.2-9b**) through 33.4 kcal mol⁻¹, resulting in a fused four-membered ring $A_2YC_5\bullet YC_3ODOb$ at 18.2 kcal mol⁻¹. The strained ring in the latter intermediate breaks the C—O bond via 4.6 kcal mol⁻¹ (**TS1.2-10b**), followed by a CO₂ elimination (**TS1.2-11b**) to $A_2YC_5\bullet$, which is further converted in Channel 3.2, see Figures 11 and 12.

3.2.4 | Formation of $A_3\bullet YC_4O_2$ Through Addition of the Oxygen Atom to Adjacent Ring (Channel 1.3)

Another reaction path available to the $A_3OO\bullet$ peroxy radical is the addition of the oxygen radical to the nearest carbon atom in the adjacent ring (**TS1.3-1**), see Figure 7. This reaction occurs via a non-strained six-membered ring requiring ca. 21 kcal mol⁻¹ and results in $A_3\bullet YC_4O_2$ at an energy of 72.1 kcal mol⁻¹. The O—O bond in $A_3\bullet YC_4O_2$ subsequently is opened over a low barrier of only 4.0 kcal mol⁻¹ (**TS1.3-2**) to the more stable intermediate at lower energy (31.7 kcal mol⁻¹) $A_2\bullet DOA_1YC_2O$, where each oxygen atom is attached to a different ring. Next, the C—C bond in the three-membered ring of $A_2\bullet DOA_1YC_2O$ is opened over a barrier of 17. kcal mol⁻¹ (**TS1.3-3**) relative to $A_2\bullet DOA_1YC_2O$ to form $A_2DOYC_6O\bullet$ containing a seven-membered ring. Four channels for consecutive reactions of $A_2DOYC_6O\bullet$ are possible, see Figure 7. Two paths occur via high energy barriers of 66 and

79.5 kcal mol⁻¹, respectively (**TS1.3-4A** and **TS1.3-4B**, see excerpt in Figure 7). Due to the high energy barriers, these two paths are not further considered in this study. The third consecutive path of $A_2DOYC_6O\bullet$ consists of bonding two carbons inside the seven-membered ring to form a five-membered ring over some 34 kcal mol⁻¹ (**TS1.3-4**), resulting in $A_2DOYC_5\bullet CDO$ at 26.3 kcal mol⁻¹, which finally dissociates into $A_2DOYC_5\bullet + CH\equiv O$ (**TS1.3-5**). The fourth path available to $A_2DOYC_6O\bullet$, see Figure 8, is the bonding of the two carbons inside the six-membered ring via **TS1.3-6** at 37 kcal mol⁻¹ to form a new three-membered ring $YC_6OA_1YC_5C\bullet DO$ at 79.9 kcal mol⁻¹. The three-membered ring in the latter breaks easily via **TS1.3-7** (9.3 kcal mol⁻¹), forming $YC_6OA_1YC_5C\bullet DO$ at 76.1 kcal mol⁻¹.

The further reaction sequence of $YC_6OA_1YC_5C\bullet DO$ consists of an exothermic CO elimination without barrier (**TS1.3-8**) to $YC_6OA_1YC_5\bullet$, see Figure 8. The latter opens the seven-membered ring over **TS1.3-9** (41.4 kcal mol⁻¹) to $YC_5A_1CDOC_3\bullet$ followed by a C₂H₂ elimination (**TS1.3-10**) with ca. 42 kcal mol⁻¹ to $YC_5A_1CDOC\bullet$. After an intramolecular H-abstraction (**TS1.3-11**), the latter species eliminates another CO over **TS1.3-12** with 23.7 kcal mol⁻¹ to the final product $YC_5A_1\bullet DC$.

Alternatively, $YC_6OA_1YC_5\bullet$ may carry out a C—C bond formation inside the seven-membered ring over **TS1.3-13** with 47.2 kcal mol⁻¹, forming a new fused but unstable four-membered ring $YC_5A_1YC_5YC_3\bullet O$. This “C₃O” cycle opens with a low barrier **TS1.3-14** and an excess of energy of 41 kcal mol⁻¹ to the intermediate $YC_5A_1YC_5\bullet CDO$, which dissociates via **TS1.3-15** to the final products as-Indacene $YC_5A_1YC_5\bullet + CH\equiv O$.

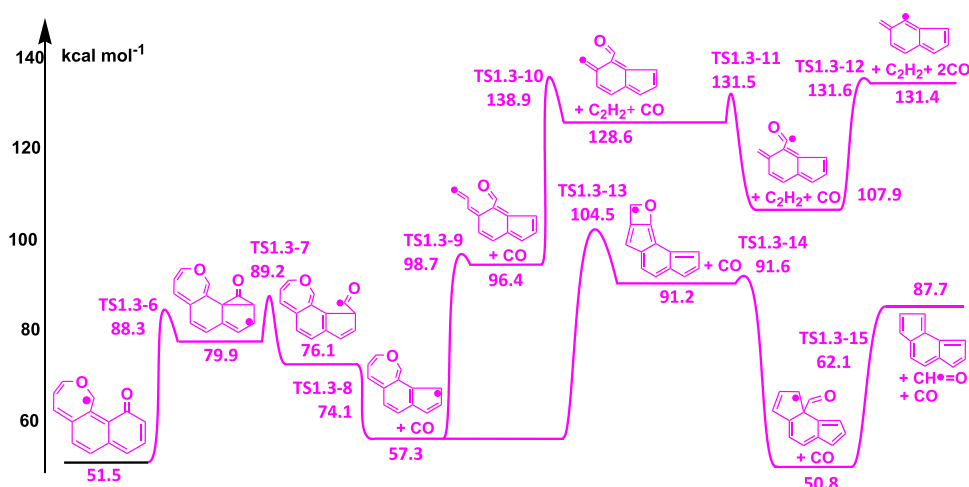


FIGURE 8 | Formation and further reactions of $A_3 \bullet YC_4O_2$ (channel 1.3 continuation).

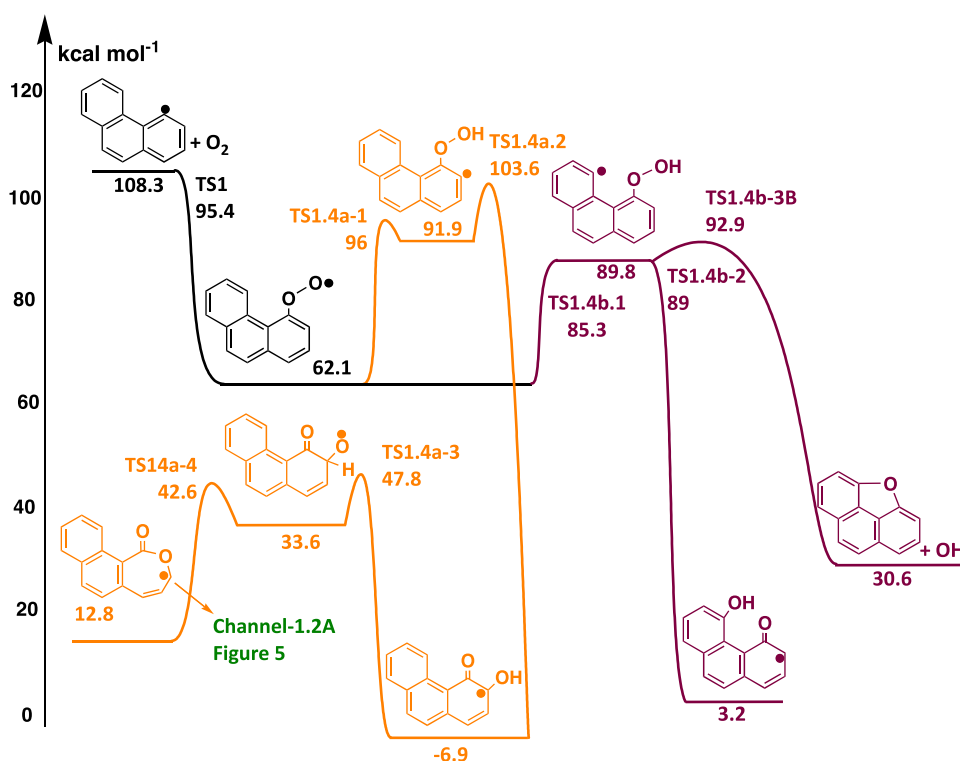


FIGURE 9 | Formation and further reactions of $A_3 \bullet OOH$ (channel 1.4a and 1.4b).

3.2.5 | Formation of $A_3 \bullet OOH$ Through Intramolecular H-abstraction by the Oxygen Atom (Channel 1.4)

Compared to the two-ring ($A_2 \bullet$) or one-ring ($A_1 \bullet$) systems, an intramolecular H-abstraction from the adjacent carbon atom via **TS1.4a-1** leads to an ortho-hydroperoxy-phenanthryl radical $A_3 \bullet OOH$ -a (see Figure 9). The energy barrier for this abstraction of about 33 kcal mol⁻¹ is still 12.3 kcal mol⁻¹ below the energy at the starting point $A_3 \bullet + O_2$ of this channel. The subsequent reaction of $A_3 \bullet OOH$ -a is governed by an O—OH bond scission followed by an exothermic shift of the OH group to the radical site in $A_3 \bullet OOH$ -a (**TS1.4a-2**) via a small barrier of ca. 12 kcal mol⁻¹. In this reaction, the cyclic hydroxyl-ketone radical $A_2A_1 \bullet OHDO$ at a low energy of -6.9 kcal mol⁻¹ is formed with some 100 kcal

mol⁻¹ excess of energy released to the system. With the available energy, $A_2A_1 \bullet OHDO$ undergoes a hydrogen shift from the OH group to the carbon radical site (see Figure 9) over **TS1.4a-3** with 55 kcal mol⁻¹ to form $A_2A_1O \bullet DO$ at 33.6 kcal mol⁻¹. The oxygen of the latter radical attacks the adjacent carbon, forming the intermediate species $A_2YCDOOC \bullet CC$ via **TS1.4a-4** with 9.0 kcal mol⁻¹. The further conversion of $A_2YCDOOC \bullet CC$ continues in Channel 1.2A, see Section 3.2.3 and Figure.

The intramolecular hydrogen abstraction from the peroxy radical $A_3OO \bullet$ can also take place from the remote six-membered ring. As illustrated in Figure 9, the abstraction of a hydrogen located in the remote third ring (facing ring) is favorable because of its geometry (**TS1.4b-1**). This H-abstraction takes place without

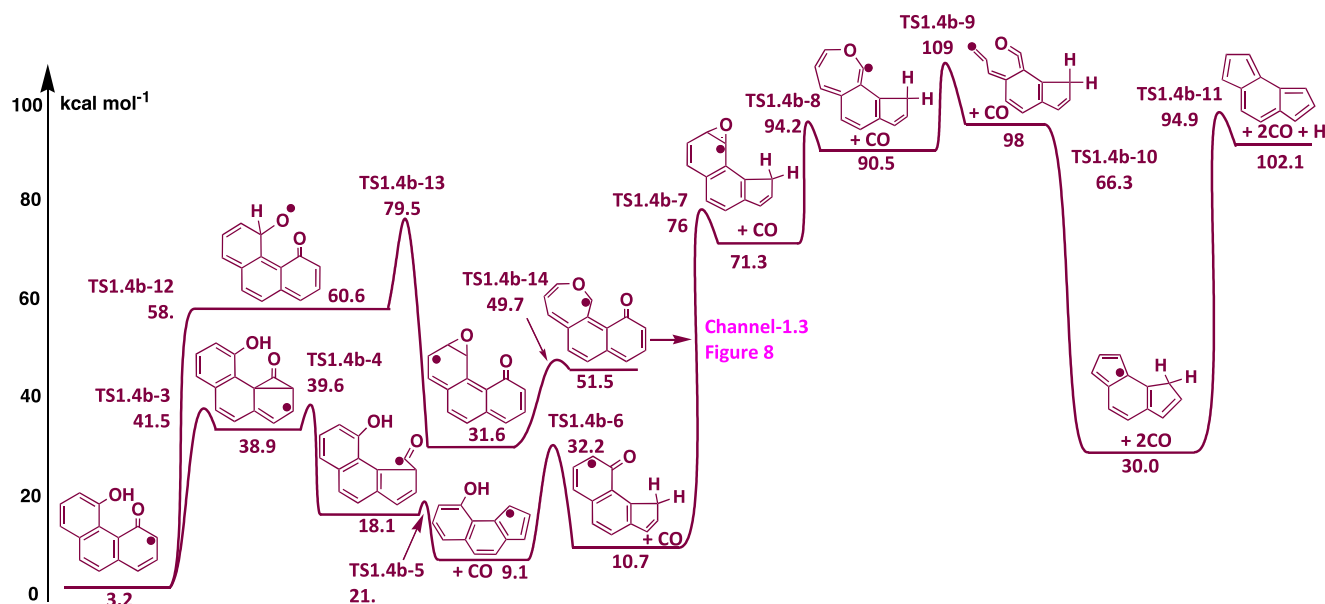


FIGURE 10 | Formation and further reactions of $A_3\bullet\text{OOH}$ (channel 1.4b continuation).

saddle point because of the non-strained six-membered ring structure. The hydroperoxide radical $A_3\bullet\text{OOH-b}$ is formed at $89.8 \text{ kcal mol}^{-1}$, which is $18.5 \text{ kcal mol}^{-1}$ below the energy at the starting point $A_3\bullet + \text{O}_2$ of this channel. During the hydrogen abstraction, the transition state **TS1.4b-1** involves a loose seven-membered ring structure in contrast to the abstraction in the five-membered ring structure occurring via **TS1.4a-1**. This explains the difference in energy required for both H-abstraction reactions. The $A_3\bullet\text{OOH-b}$ isomer undergoes a second intramolecular shift of the OH group of the peroxy group to the facing radical site. This reaction takes place without barrier (**TS1.4b-2**) and releases $86.6 \text{ kcal mol}^{-1}$, forming an isomer $A_2\text{OHA}_1\bullet\text{DO}$ at $3.2 \text{ kcal mol}^{-1}$. The ortho-hydroperoxy-phenanthryl radical $A_3\bullet\text{OOH-b}$ can alternatively eliminate an OH via a low barrier of $3.1 \text{ kcal mol}^{-1}$ (**TS1.4b-3B**) to form the stable $A_3\text{YC}_4\text{O}$.

The available energy released during the formation of $A_2\text{OHA}_1\bullet\text{DO}$ opens two possible consecutive paths (Figure 10). The first path is governed by a C—C bond formation inside one ring, forming a three-membered ring $A_2\text{OHYC}_5\bullet\text{YC}_3\text{DO}$ via **TS1.4b-3** with a ca. 38 kcal mol^{-1} energy barrier. Similar to the channels described above, the strained three-membered ring “ YC_3DO ” opens by breaking the C—O bond via **TS1.4b-4** (only $0.7 \text{ kcal mol}^{-1}$), resulting in $A_2\text{OHYC}_5\text{C}\bullet\text{DO}$ at a calculated low energy of $18.3 \text{ kcal mol}^{-1}$. This species eliminates CO immediately (via only $2.7 \text{ kcal mol}^{-1}$ **TS1.4b-5**) to $A_2\text{OHYC}_5\bullet$. The latter proceeds by transferring the H of the OH group to the facing radical site of the 5-membered ring (**TS1.4b-6**) forming $\text{ODA}_2\bullet\text{YC}_5$. This step is followed by a C—O bond formation (**TS1.4b-7**) to a three-membered ring in the intermediate $\text{YC}_5\text{A}_2\bullet\text{YC}_2\text{O}$ via a relatively high energy barrier of 65 kcal mol^{-1} . This species opens the three-membered ring (**TS1.4b-8**) to $\text{YC}_5\text{A}_1\text{YC}_6\bullet\text{O}$, lying some 20 kcal mol^{-1} higher than the previous radical. The subsequent reactions of the latter species are ring opening via **TS1.4b-9** ($18.5 \text{ kcal mol}^{-1}$) followed by a barrierless CO elimination and a 5-membered-ring closure (**TS1.4b-10**) forming $\text{YC}_5\text{A}_1\text{YC}_5\bullet$ and finally a hydrogen elimination (**TS1.4b-11**) resulting in a stable $\text{YC}_5\text{A}_1\text{YC}_5$ and H.

The second possible path enabled by the excess of energy for $A_2\text{OHA}_1\bullet\text{DO}$ consists of the hydrogen transfer of the OH group to the same carbon atom via **TS1.4b-12** (55 kcal mol^{-1}), forming an intermediate $A_2\text{DOA}_1\bullet\text{O}$ at $60.6 \text{ kcal mol}^{-1}$ with a radical site located on the oxygen. The oxygen can bond to the adjacent carbon by overcoming ca. 19 kcal mol^{-1} (**TS1.4b-13**) and conducting to $A_2\text{DOA}_1\bullet\text{YC}_2\text{O}$ at $31.6 \text{ kcal mol}^{-1}$. The latter undergoes ring opening of the three-membered ring by breaking the C—C bond via **TS1.4b-14** ($18.1 \text{ kcal mol}^{-1}$) to $A_2\text{DOYC}_6\text{O}\bullet$. Subsequent reactions of $A_2\text{DOYC}_6\text{O}\bullet$ occur in Channel 1.3, see Section 3.2.4 and in Figure 7.

3.2.6 | Formation of $a_3\bullet\text{DO}$ Through RO—O Bond Cleavage (Channel 2)

The O—O scission of the peroxy radical $A_3\text{OO}\bullet$, conducting to $\text{A}3\text{O}\bullet + \text{O}$, labeled as Channel 2, takes place with an energy barrier of 31 kcal mol^{-1} above the stabilized $\text{A}3\text{OO}\bullet$. This energy barrier is similar to other systems like $\text{A}_2\bullet + \text{O}_2$ or $\text{A}_1\bullet + \text{O}_2$ as reported in [3, 4]. Comparable to the $\text{A}_2\bullet + \text{O}_2$ system, the radical $\text{A}_3\text{O}\bullet$ rearranges by forming a C=O double bond to a more stable $\text{A}_3\bullet\text{DO}$ at $39.6 \text{ kcal mol}^{-1}$. This value is in good agreement with the value of $37.89 \text{ kcal mol}^{-1}$ from ref. [7]. Subsequent reactions of the phenanthrene oxyradical $\text{A}_3\text{O}\bullet$ or $\text{A}_3\bullet\text{DO}$ are examined and discussed in Section 3.3.

3.3 | Reactions of the Phenanthryl Radical $A_3\bullet$ ($\text{C}_{14}\text{H}_9\bullet$) With O

The main reaction channels describing the addition of an oxygen atom to $\text{A}_3\bullet$ to $\text{A}_3\text{O}\bullet$ are illustrated in Figure 2. Due to its higher stability, the $\text{A}_3\text{O}\bullet$ radical rearranges to $\text{A}_3\bullet\text{DO}$. All further reactions of $\text{A}_3\text{O}\bullet$ conduct mainly to a radical, CO and acetylene. The primary pathways resulting from the subsequent reactions of the peroxy radical $\text{A}_3\text{O}\bullet$ ($\text{A}_3\bullet\text{DO}$), see Figure 1, include:

Channel 3: Addition of an oxygen atom to $A_3\cdot$, forming $A_3O\cdot$ and $A_3\cdot DO$.

Channel 3.1: Further reactions of $A_3\cdot DO$.

Channel 3.2: Further reactions of $A_3\cdot DO$ via elimination of CO.

Channel 3.3: Addition of an oxygen atom to $A_3\cdot DO$, forming $A_3O\cdot DO$.

These reaction channels are described in detail in the following sections.

3.3.1 | Addition of an Oxygen Atom to $A_3\cdot$ Forming $A_3O\cdot$ and $A_3\cdot DO$ (Channel 3)

The direct addition of an oxygen atom to the phenanthryl radical $A_3\cdot$ (TS3) is the second reaction path resulting in the formation of $A_3\cdot DO$ (see Figure 1 and illustration in Table A1). This addition reveals a barrier of 16.3 kcal mol⁻¹ relative to $A_3\cdot + O$, whereas the formation of $A_3\cdot DO$ through O—O dissociation of $A_3OO\cdot$ (TS2) necessitates about 31 kcal mol⁻¹. It is, however, important to point out that the energy at the starting point of this channel $A_3\cdot + O$ is 166 kcal mol⁻¹, whereas $A_3OO\cdot$ is much lower at 62.7 kcal mol⁻¹. These two different levels of energy may be determinant for the occurrence of these two competitive pathways; nevertheless, both reactions are considered.

3.3.2 | Further Reactions of $A_3\cdot DO$ (Channel 3.1)

The oxyradical $A_3\cdot DO$ undergoes an intramolecular addition of the oxygen to the adjoining carbon forming a three-membered ring $A_3\cdot YC_2O$ over a barrier of 60.8 kcal mol⁻¹ (TS3.1-1) relative to $A_3\cdot DO$, see Figure 11. This high barrier may be explained by the scission of the strong C=O double bond. The latter radical ($A_3\cdot YC_2O$) formed at 96.4 kcal mol⁻¹ opens barrierless the strained three-membered ring (TS3.1-2) by breaking the C—C bond, resulting in $A_2YC\cdot OC_3$ at 115.3 kcal mol⁻¹. The subsequent reactions of $A_2YC\cdot OC_3$ comprise a ring opening requiring ca. 17 kcal mol⁻¹ (TS3.1-3) to $A_2DCDOC_3\cdot$ at 115 kcal mol⁻¹, followed by a dissociation reaction over an energy barrier of 47 kcal mol⁻¹ (TS3.1-4) to the unstable $A_2DCDOC\cdot$ and C_2H_2 . $A_2DCDOC\cdot$ rearranges via a barrier of 4.7 kcal mol⁻¹ (TS3.1-5) and forms a C—C bond conducting to a four-membered ring $A_2YC_4\cdot DO$ at lower energy.

3.3.3 | Further Reactions of $A_3\cdot DO$ via Elimination of CO (Channel 3.2)

Similar to the $A_2\cdot + O_2$ system reported in previous work [4] and by Zhou et al. [31], a second and more plausible reaction of the $A_3\cdot DO$ is illustrated in Figure 12. In the $A_3\cdot DO$ radical, a C—C bond takes place, forming a fused pentacyclic radical over a lower barrier of 47.6 kcal mol⁻¹ (TS3.2-1) and resulting in $A_2YC_5\cdot YC_3DO$ at 85.1 kcal mol⁻¹. This barrier is very similar and varies by only 10 kcal mol⁻¹ from that calculated for the $A_2\cdot + O_2$ system [4]. The pentacyclic radical $A_2YC_5\cdot YC_3DO$ with the adjacent three-membered ring rearranges almost barrierless

(TS3.2-2) to a lower energy compound by opening the strained three-membered cycle and resulting in $A_2YC_5C\cdot DO$, which lies some 20 kcal mol⁻¹ lower than $A_2YC_5\cdot YC_3DO$. This latter radical proceeds to CO elimination (TS3.2-3) over only 3.3 kcal mol⁻¹ (28.2 kcal mol⁻¹ above $A_3\cdot DO$) to the indenyl radical $A_2YC_5\cdot$ and CO, lying 16.1 kcal mol⁻¹ above the $A_3\cdot DO$ radical. It is interesting to point out that the values of the barriers of TS3.2-2 and TS3.2-3 in this system are identical to the corresponding transition states in the $A_2\cdot + O_2$ system.

Figure 12 depicts the energy diagram for the addition of an oxygen atom to the cyclopentadienyl radical site of $A_2YC_5\cdot$. This addition occurs barrierless (TS3.2-4) and releases some 66 kcal mol⁻¹ while forming $A_2YC_5O\cdot$, which lies at 74.4 kcal mol⁻¹. Here again, we note that the excess of energy released is the same as that involved in the corresponding reaction of the $A_2\cdot + O_2$ system [4]. For the $A_2YC_5O\cdot$ intermediate, two subsequent reaction channels are available. The oxygen radical site of $A_2YC_5O\cdot$ bonds to the adjacent carbon over only 3.2 kcal mol⁻¹ (TS3.2-5), resulting in a fused $A_2YC_5\cdot YC_2O$ at 68.2 kcal mol⁻¹. Due to its strained structure, the latter rearranges to an energetically lower isomer $A_2YC_5\cdot O$ over 18 kcal mol⁻¹ (TS3.2-6). $A_2YC_5\cdot O$ breaks the C—O bond of its $Y(C_5\cdot O)$ ring (TS3.2-7) to the isomer $A_2CDOC_2\cdot$ at 82.8 kcal mol⁻¹. This last intermediate $A_2CDOC_2\cdot$ is converted by a series of eliminations leading to alpha-naphthyl, CO, and C_2H_2 as illustrated in Figure 12.

The second plausible path of $A_2YC_5O\cdot$ is the electron rearrangement through its resonance structure (TS3.2-11 over 2.3 kcal mol⁻¹) to an energetically lower isomer $A_2\cdot YC_5DO$ at 44.6 kcal mol⁻¹, followed by the ring opening of the five-membered ring (TS3.2-12) through some 14 kcal mol⁻¹. The resulting intermediate $A_2C_2C\cdot DO$ continues dissociation to alpha-naphthyl, CO, and C_2H_2 via Channel 1.2A, see Figure 4.

As a trial, the addition of O_2 to $A_2YC_5\cdot$ has been tested. The addition occurs over only some 3 kcal mol⁻¹ barrier (TS3.3-4-O2, see illustration in Table A1) and results in a peroxy radical, $A_2YC_5O_2\cdot$ at 74.3 kcal mol⁻¹. A preliminary homogeneous-reactor simulation showed that the $A_2YC_5O_2\cdot$ peroxy radical is formed in negligible concentration and, therefore, further investigation of this reaction path has not been performed.

3.3.4 | Addition of an Oxygen Atom to $A_3\cdot DO$ Forming Para- $A_3O\cdot DO$ (Channel 3.3)

Similar to the previously $A_2\cdot + O_2$ investigated system [4], and in order to explore all possible reactions of $A_3\cdot$, the addition of an oxygen atom to the $A_3\cdot DO$ radical (TS3.3) has been investigated (see Figures 13–15). Based on the results of the $A_2\cdot + O_2$ system, addition of the oxygen atom in ortho-position relative to the C—O site results in the same intermediate species as those appearing in Channel 1.1 (Figure 3) and Channel 1.2A (Figure 4), compare Sections 3.2.2 and 3.2.3.

The para-addition of the O-atom to $A_3\cdot DO$ is with 61.4 kcal mol⁻¹ exothermic, which is identical to the corresponding oxygen atom addition in the $A_2\cdot + O_2$ system [4]. Due to the available excess of energy, the formed para- $A_3O\cdot DO$ easily forms two C—O bonds to

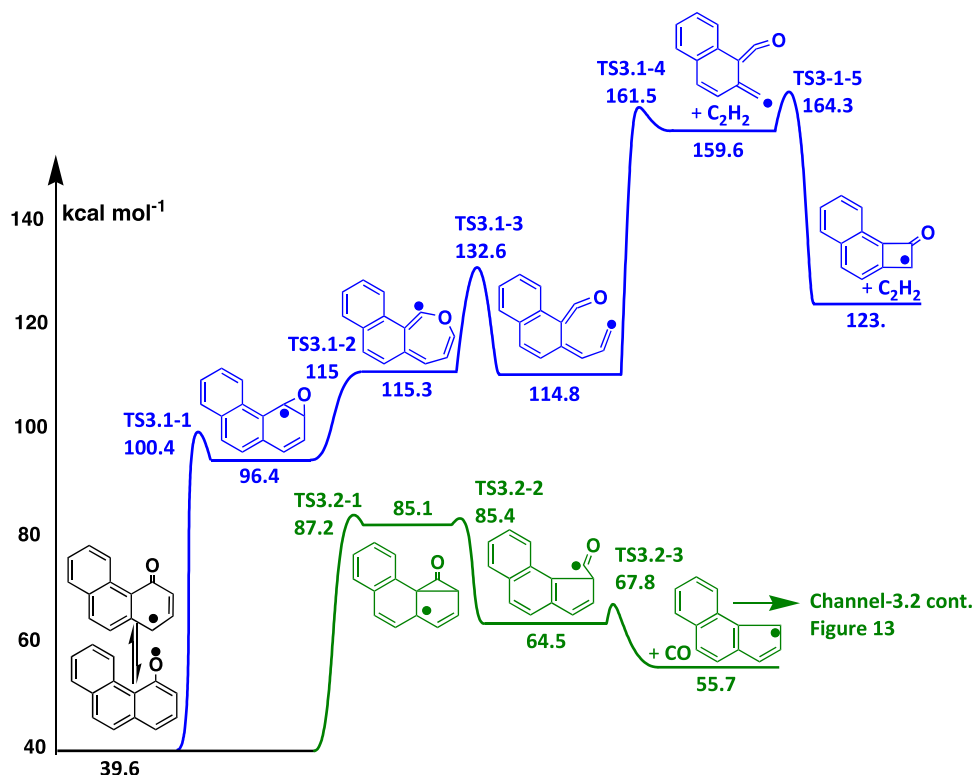


FIGURE 11 | Formation and further reactions of $A_3\bullet DO$ (channel 3.1 and channel 3.2).

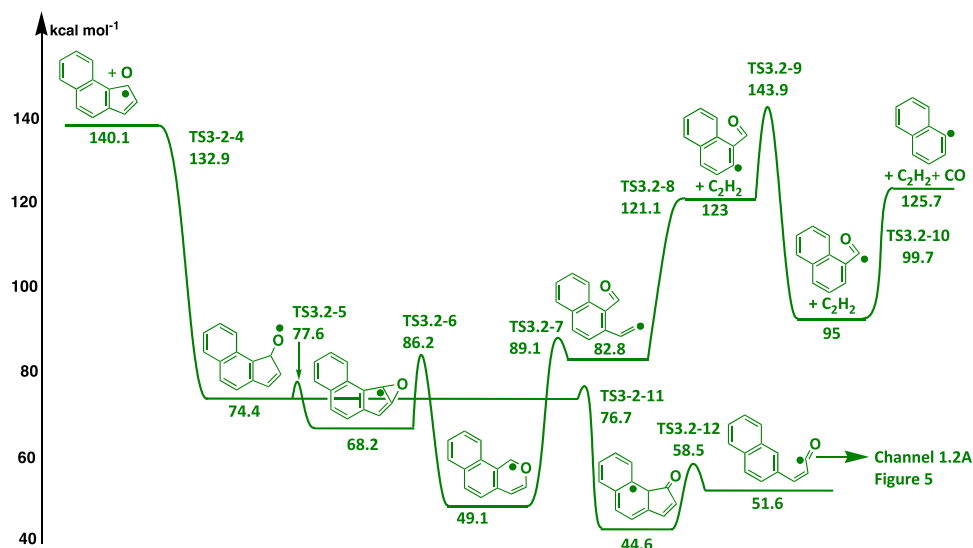


FIGURE 12 | Oxidation of $A_2YC_5\bullet$ to formation and further reactions of $A_2YC_5O\bullet$ (channel 3.2 continuation).

the carbon atoms located on the right and left side of the oxygen radical site. This results in two isomers with three-membered rings, $A_3DOC\bullet YC_2O$ over only 5.3 kcal mol⁻¹ via **TS3.3-1a** and $A_3\bullet DOYC_2O$ -b via **TS3.3-1b** over 8.1 kcal mol⁻¹, see Figure 13. The para- $A_3O\bullet DO$ may undergo an H-abstraction (**TS-H**) requiring 8.2 kcal mol⁻¹ to form the stable molecule 1,4-phenanthrenedione A_2ODA_1DO and H. Addition of O_2 to the para- $A_3O\bullet DO$ (**TS+O2**) results in $A_2ODA_1DO + HOO\bullet$.

Figure 14 illustrates the subsequent reactions of the isomer $A_3DOC\bullet YC_2O$, which opens the three-membered ring by break-

ing the C—O bond to $A_2YCDOC_2OC\bullet$ formed at about the same level of energy of 30.2 kcal mol⁻¹ and over a barrier of ca. 10 kcal mol⁻¹ (**TS3.3-2a**). Two pathways are available to this intermediate. The seven-membered ring opens via a barrier of 38 kcal mol⁻¹ (**TS3.3-3a**), forming the intermediate $A_2CDOCDOC_2\bullet$ at 49.3 kcal mol⁻¹. The subsequent reactions of the latter compound are C_2H_2 elimination (via **TS3.3-4a**, 22.3 kcal mol⁻¹) followed by CO elimination (via **TS3.3-5a**, 26.1 kcal mol⁻¹) and resulting in the beta- $A_2\bullet CDO$ intermediate, the further dissociation reactions of which to CO and beta- $A_2\bullet$ occur analogously to those of the alpha- $A_2\bullet CDO$ as described in Section 3.2.3 (see Figure 5).

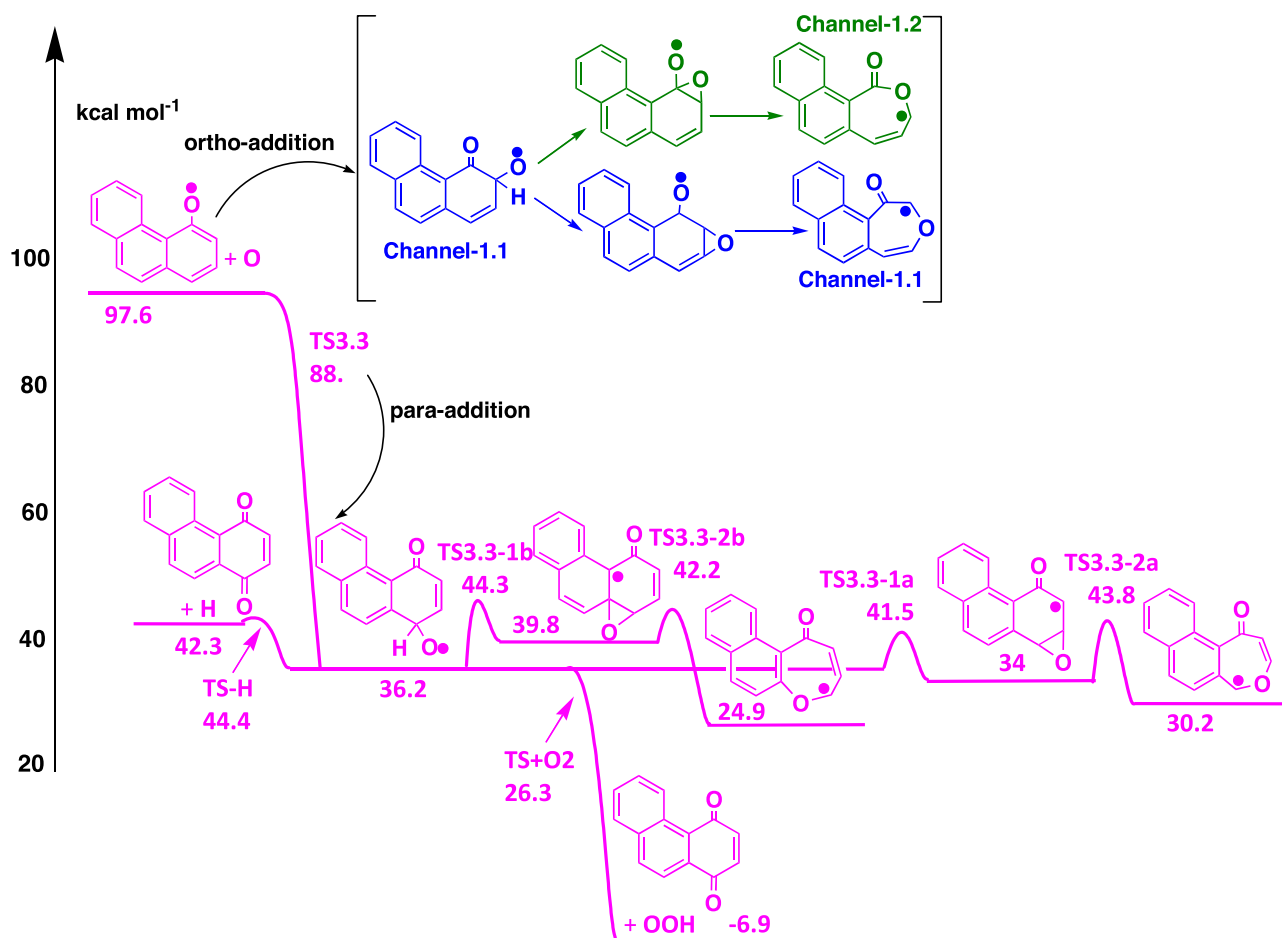


FIGURE 13 | Oxidation of $A_3\bullet DO$; formation and further reactions of $A_3O\bullet DO$ (Channel 3.3).

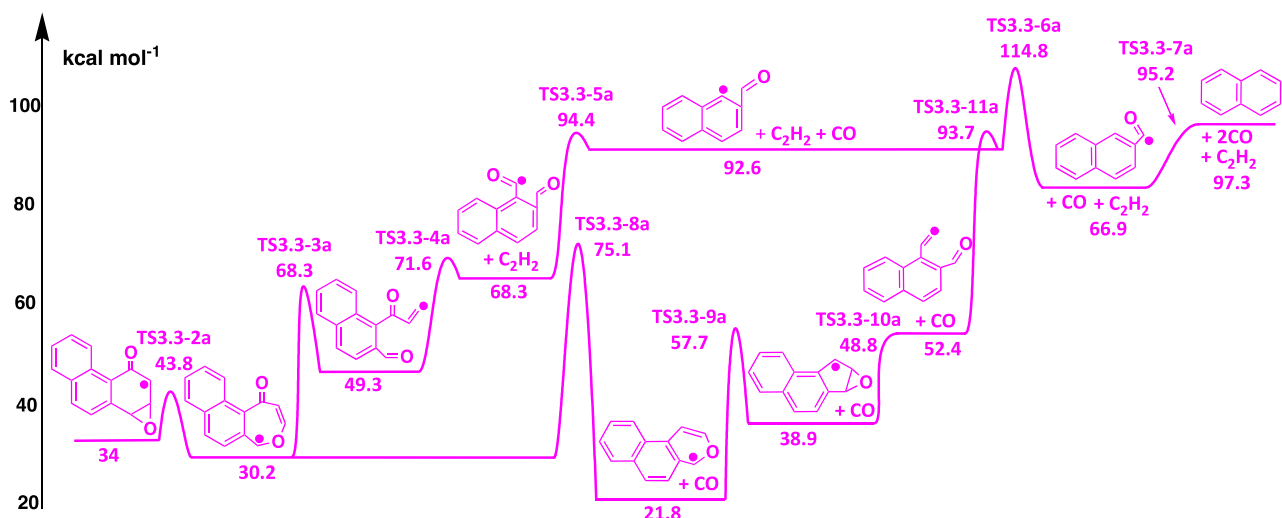


FIGURE 14 | Further reactions of $A_3O\bullet DO$ (Channel 3.3, subsequent reactions of $A_3DOC\bullet YC_2O$).

The second possible path of the $A_2YCDOC_2OC\bullet$ intermediate consists of a CO elimination (TS3.3-8a), which possibly can take place using the available energy released previously by forming para- $A_3O\bullet DO$ at 36.2 kcal mol⁻¹. This is followed by the formation of a three-membered ring in $AYC_5\bullet YC_2O$ over some 36 kcal mol⁻¹ (TS3.3-9a). The simultaneous ring opening/CO

elimination reaction of this radical requires ca. 10 kcal mol⁻¹ (TS3.3-10a), which is followed by C_2H_2 elimination (TS3.3-11a) via 41.3 kcal mol⁻¹ to beta- $A_2C\bullet DO$.

Figure 15 illustrates the subsequent reactions of the second isomer $A_3\bullet DOYC_2O$ -b, which undergoes a C—C bond scission

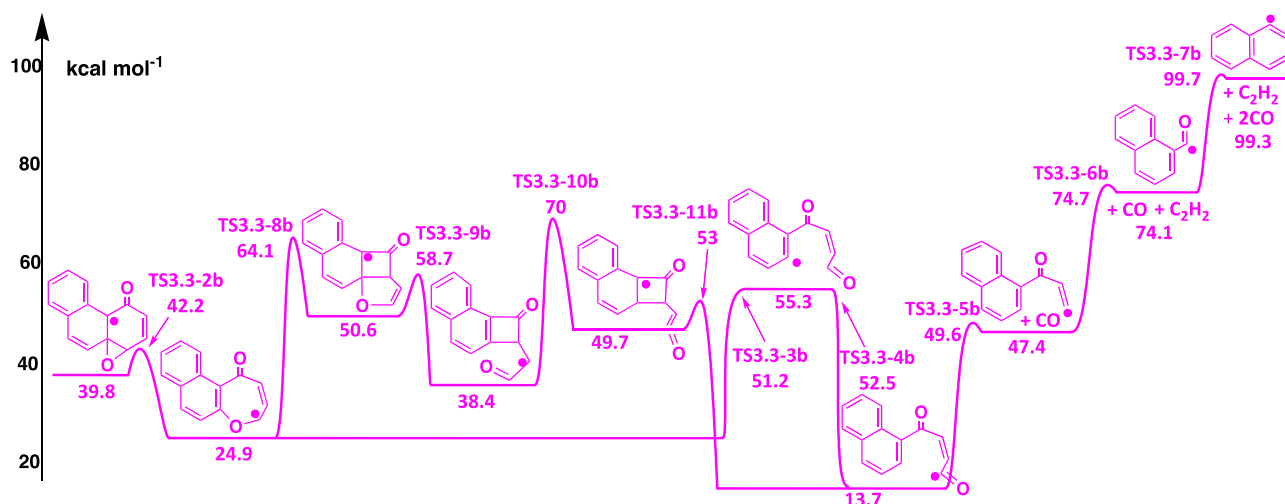


FIGURE 15 | Further reactions of $A_3O\bullet DO$ (Channel 3.3, subsequent reactions of $A_3\bullet DOYC_2O-b$).

(**TS3.3-2b**) by opening the strained three-membered ring via a low 2.4 kcal mol⁻¹ barrier to a seven-membered ring intermediate $A_2YCDOC_2C\bullet O$ at 24.9 kcal mol⁻¹. In a first possibility, the ring opens by breaking the C—O bond (**TS3.3-3b**) without saddle point to $A_2\bullet CDOC_3DO$ at 55.3 kcal mol⁻¹, followed by a barrierless hydrogen migration (**TS3.3-4b**) to a more favorable compound $A_2CDOC_3\bullet DO$ at lower energy, releasing 42 kcal mol⁻¹. With this available excess of energy, a series of dissociation reactions follow (**TS3.3-5b** to **TS3.3-7b**) to the final products alpha- $A_2\bullet$, CO, and C_2H_2 . In a second possibility, $A_2YCDOC_2C\bullet O$ reacts through the formation of a C—C bond inside the seven-membered ring (**TS3.3-8b**) via 39.2 kcal mol⁻¹, forming $A_2YC_4OYC_4\bullet DO$ at 50.6 kcal mol⁻¹. The latter intermediate opens the five-membered ring (**TS3.3-9b**) to a compound $A_2YC_4\bullet DOC_2O$ at a lower level of energy of 38.4 kcal mol⁻¹, followed by an intramolecular H-transfer (**TS3.3-10b**) and finally by the opening of the four-membered ring (**TS3.3-11b**) over a barrier of only 3.3 kcal mol⁻¹ to $A_2CDOC_3\bullet DO$ at 13.7 kcal mol⁻¹ (see Figure 15).

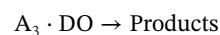
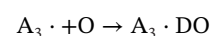
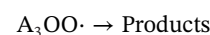
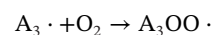
4 | Kinetic Calculations

4.1 | Reaction Rate Coefficients

Using the program ThermKin [25], the forward rate constants $k(T)$ of the elementary reactions, based on the canonical transition state theory (CTST), are determined. The reaction rate coefficients are reported in the modified Arrhenius form

$$k = A \cdot T^b \cdot \exp(-E_A/RT) \quad (1)$$

and listed in Table 2 for the temperature range from 300 to 1500 K. The reaction rate coefficients listed in Table 2 are for the initiation and first subsequent reactions only. The reaction rate coefficients for the complete mechanism comprising all reactions illustrated in Figures 1–15 are listed in Supporting Information 3. Similar to the oxidation of the naphthyl radical ($A_2\bullet + O_2$) reported in previous work [4], the high-pressure-limit reaction rate coefficients for the forward reactions of the reaction system $A_3\bullet + O_2 / A_3\bullet + O$ as illustrated in Figures 4–16, are given:



In order to adjust the nomenclature to the CHEMKIN format, all radicals labeled in Section 3 by “•” are written as “J” in Table 1. Also, the elemental composition of the different species in Table 2 is no longer written with subscripts.

4.2 | QRRK/Master-Equation Analysis

As denoted in Section 2.2, multi-channel, multi-frequency QRRK calculations with master equation analysis have been carried out as a first step for the primary subsequent reactions of $A_3OO\bullet$, see Figures 1 and 2. The reaction rate coefficients as a function of temperature and pressure are calculated to characterize fall-off and to identify dominant reaction paths. The data illustrated in the following were calculated for the temperature range of 800 to 1500 K and pressures ranging from 0.01 to 1 atm, which are relevant for the considered reaction conditions, see Section 1.

Figure 16 illustrates that the reaction rate coefficient for the ipso-addition (first reaction of Channel 1.2) is largest for the considered temperature and pressure range. The intramolecular H-abstraction (Channel 1.4b) is also important, followed by the formation of the relatively stable $A_3\bullet YC_4O_2$ (Channel 1.3) and by the RO—O cleavage (Channel 2). The reaction rate coefficients increase with increasing temperature and pressure. At temperatures above 1000 K, we note a competition between the formation of $A_3\bullet YC_4O_2$ and the dissociation reaction $A_3O\bullet + O$. The reaction rate coefficients for the Channel 1–4A and 1.1 are some orders of magnitude lower at all temperatures and pressures. The values of the rate coefficients are in good accordance with the values from CTST, see Table 2. The extension of multi-channel, multi-

TABLE 2 | Calculated reaction rate coefficients^a for the reactions discussed in Section 3. In Table 2, change all subscripts in normal text. e.g. A₃J + O₂ = A₃OOJ. It is written in the text that elemental composition is no longer written with subscripts.

No	Reaction	<i>A</i>	<i>b</i>	<i>E_A</i>
Channel 1				
1	A ₃ J + O ₂ = A ₃ OOJ	4.13E+00	3.0	−1.56
Channel 1.1				
Reactions illustrated in Figure 3				
2	A ₃ OOJ = A ₃ JYC ₂ O ₂	2.55E+11	0.26	36.59
3	A ₃ JYC ₂ O ₂ = A ₃ OJCDO	4.64E+12	0.2	−3.19
4	A ₃ OJCDO = A ₂ YCDOOCJ	5.61E+12	−0.1	9.42
5	A ₃ OJCDO = A ₃ DOYC ₂ OC	2.01E+13	−0.3	4.39
Channel 1.2				
16	A ₃ OOJ = A ₃ JYCO ₂	3.34E+11	0.31	21.16
Reactions illustrated in Figure 4				
Channel 1.2A				
17	A ₃ JYCO ₂ = A ₂ YCDOOCJ	9.68E+12	0.0	32.1
18	A ₂ YCDOOCJ = A ₂ YC ₅ JYCA	5.40E+11	0.3	29.11
21	A ₂ YCDOOCJ = A ₂ C ₃ OCJDO	8.87E+11	0.2	27.29
Reactions illustrated in Figure 6				
Channel 1.2B				
33	A ₃ JYCO ₂ = A ₂ YOCDO CJ	1.24E+13	0.2	5.55
34	A ₂ YOCDO CJ = A ₂ DOC ₄ JO	2.67E+14	−0.9	29.23
40	A ₂ YOCDO CJ = A ₂ YC ₅ JYCB	4.77E+11	0.2	33.90
Channel 1.3				
Reactions illustrated in Figure 7				
43	A ₃ OOJ = A ₃ JYC ₄ O ₂	8.99E+10	0.18	21.69
44	A ₃ JYC ₄ O ₂ = A ₂ JDOA ₁ YC	2.15E+12	0.32	4.43
Channel 1.4				
Channel 1.4a				
Reactions illustrated in Figure 9				
59	A ₃ OOJ = A ₃ JOOH*A	2.56E+10	0.69	33.36
60	A ₃ JOOH*A = A ₂ A ₁ JOHDO	9.42E+11	−0.63	12.63
Channel 1.4b				
Reactions illustrated in Figure 9				
63	A ₃ OOJ = A ₃ JOOH*B	7.43E+09	0.74	22.65
64	A ₃ JOOH*B = A ₃ YC ₄ O + OH	1.20E+10	1.25	3.09
65	A ₃ JOOH*B = A ₂ OHA ₁ JDO	2.09E+10	0.04	−0.34
Channel 2				
78	A ₃ OOJ = A ₃ OJ + O	1.43E+12	0.4	31.32
Channel 3				
79	A ₃ J + O = A ₃ OJ	6.79E+05	1.6	15.22
Channel 3.1				
Reactions illustrated in Figure 11				
80	A ₃ OJ = A ₃ JYC ₂ O	2.65E+12	0.2	61.26
85	A ₃ OJ = A ₂ YC ₅ JYC ₃	4.80E+11	0.5	47.96

(Continues)

TABLE 2 | (Continued)

No	Reaction	<i>A</i>	<i>b</i>	<i>E_A</i>
Channel 3.2				
Reactions illustrated in Figure 12				
88	$A_2YC_5J + O = A_2YC_5OJ$ Ref. [32]	1.00E+10	0.0	0.0
89	$A_2YC_5OJ = A_2YC_5JYC_2$	1.13E+13	−0.1	7.24
95	$A_2YC_5OJ = A_2JYC_5DO$	1.06E+12	0.3	6.15
Channel 3.3				
Reactions illustrated in Figure 13				
98	$A_3OJ + O = A_3OJDO$	1.84E+05	1.8	−19.85
99	$A_3OJDO = A_2ODA_1DO + H$	4.60E+10	1.1	8.32
100	$A_3OJDO + O_2 = A_2ODA_1DO + HO_2$	1.70E+02	2.8	−10.38
101	$A_3OJDO = A_3DOCJYC_2$	8.30E+12	0.0	5.97
	$A_3OJDO = A_3JDOYC_2O$	4.68E+12	0.0	8.71

Note: For CHEMKIN use a radical labeled with “J”. The elemental composition of the different species is no longer written with subscripts (The unit of *A* in s, cm³, mol, and K depending on the order of reaction and *b*, the unit of *E_A* is kcal·mol^{−1}).

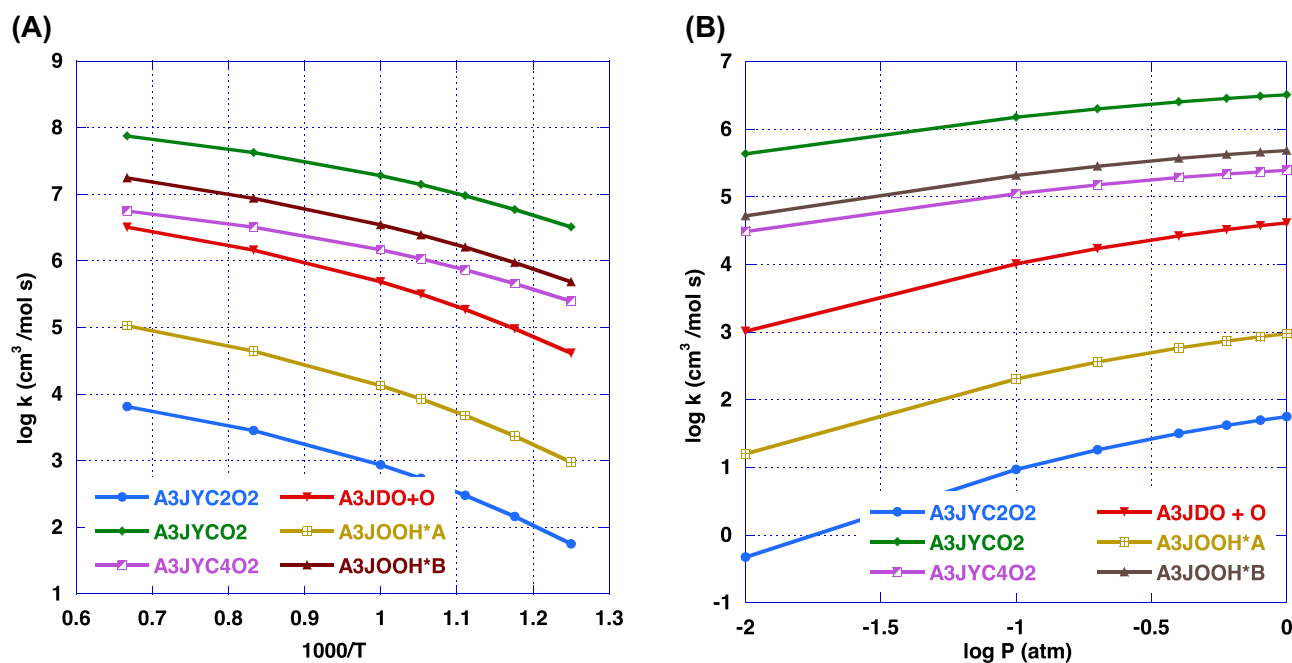


FIGURE 16 | Reaction rate coefficients for the primary subsequent reactions of $A_3OO\bullet$; the single reactions are labeled by the products; left: temperature dependence at 1 atm; right: pressure dependence at 800 K.

frequency QRRK calculations with master equation analysis to the whole system of reactions is in preparation.

5 | Summary and Conclusions

In this study, several possible pathways of the reaction system $A_3\bullet + {}^3O_2$ and $A_3\bullet + O$ are investigated using DFT (B3LYP, M06, and APFD) quantum chemistry calculations as part of a comprehensive reaction mechanism of the oxidation of phenanthrene. The reaction channels were investigated down to the next smaller PAH-radical (naphthyl $A_2\bullet$) and the corresponding

reaction products. The thermodynamic properties (enthalpies, entropies, and heat capacities) of the involved intermediates, transition state structures, and products are determined and reported in this work.

Similar to the oxidation of the naphthyl radical ($A_2\bullet + {}^3O_2$) reported in a previous study [4], a peroxy radical $A_3OO\bullet$ is formed with an excess of energy around 45 kcal mol^{−1}. Six subsequent channels for the decomposition and oxidation of $A_3OO\bullet$ are investigated. We note again that, like for $A_2\bullet + {}^3O_2$, the main and dominant path is governed by the addition of the terminal oxygen of the peroxy group to the same carbon atom (ipso addition) over

a 21 kcal mol⁻¹ energy barrier, which is 25 kcal mol⁻¹ below the energy of the starting point of this channel.

The reaction rate coefficients for the several reactions involved in the A₃• + ³O₂ system have been determined and enable the identification of the dominant reaction paths.

All six investigated reaction channels, except Channel 1.3, conduct to α-A₂•, CO, CO₂, and C₂H₂ as main products. Minor products are β-A₂•, A₂YC₅•, A₂OHYC₅•, A₃YC₄O and ODA₂YC₅•. This product distribution supports the hypothesis that in the oxidation of PAHs, the pathways producing CO, CO₂, C₂H₂, and finally C₆H₅• may constitute a repetitive reaction sequence for the successive diminution of six-membered rings in larger polycyclic aromatic hydrocarbons.

Nomenclature

Nomenclature in this work is as follows:

Y(A)	indicates a cyclic structure
A• or AJ	represents a radical site on the structure
D	is a double bond (e.g., CDO is C=O)
TS	is a transition state structure

For example, Y(C₅) DO represents a cyclic five-membered carbon ring with a double bond to an oxygen on a ring carbon.

Acknowledgments

Open access funding enabled and organized by Projekt DEAL.

Conflicts of Interest

The authors declare no conflicts of interest

Data Availability Statement

The data that support the findings of this study are available from the corresponding author upon reasonable request.

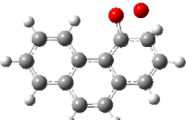
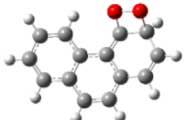
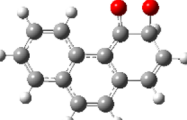
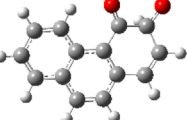
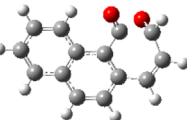
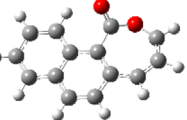
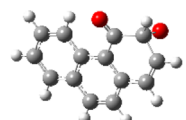
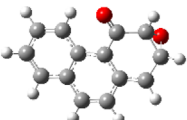
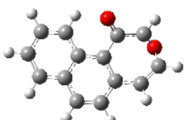
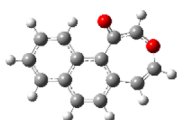
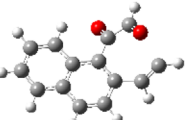
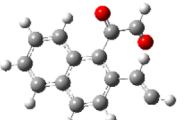
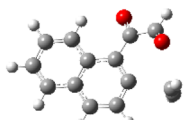
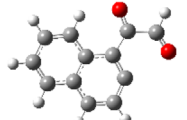
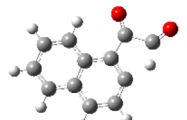
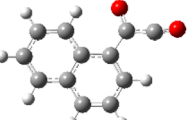
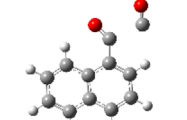
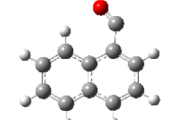
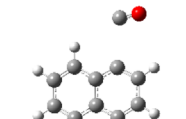
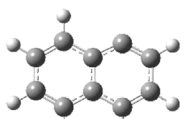
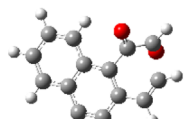
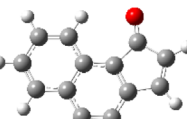
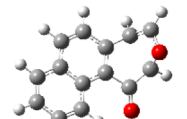
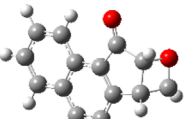
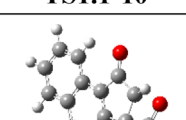
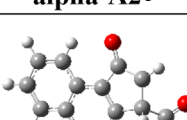
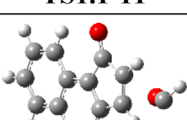

References

1. F. P. Hagen, D. Kretzler, T. Häber, H. Bockhorn, R. Suntz, and D. Trimis, "Carbon Nanostructure and Reactivity of Soot Particles From Non-intrusive Methods Based on UV-VIS Spectroscopy and Time-Resolved Laser-Induced Incandescence," *Carbon* 182 (2021): 634–654.
2. N. Sebbar, H. Bockhorn, and D. Trimis, "Oxidation of Polycyclic Aromatic Hydrocarbons: Evidence of Similarities in Thermochemical Properties and Reaction Paths," *Combustion Science and Technology* 195 (2023): 3341–3356.
3. N. Sebbar, H. Bockhorn, and J. W. Bozzelli, "Thermodynamic Properties of the Species Resulting From the Phenyl Radical With O₂ Reaction System," *International Journal of Chemical Kinetics* 40 (2008): 583–604.
4. N. Sebbar, H. Bockhorn, and D. Trimis, "Oxidation of the 1-Naphthyl Radical C₁₀H₇• With Oxygen: Thermochemistry, Kinetics and Dominant Reaction Pathways," *International Journal of Chemical Kinetics* 56 (2024): 210–232.
5. R. Abhijeet, Y. Y. Seung, C. Dongkyu, T. Russell, and H. C. Suk, "Structural Effects on the Oxidation of Soot Particles by O₂: Experimental and Theoretical Study," *Combustion and Flame* 160 (2013): 1812–1826.
6. R. Abhijeet, G. R. da Silva, and H. C. Suk, "Reaction Mechanism for the Free-Edge Oxidation of Soot by O₂," *Combustion and Flame* 159 (2012): 3423–3436.
7. D. E. Edwards, X. You, D. Y. Zubarev, W. A. Lester, and M. Frenklach, "Thermal Decomposition of Graphene Armchair Oxyradicals," *Proceedings of the Combustion Institute* 34 (2013): 1759–1766.
8. J. T. Barbas, M. E. Sigman, and R. Dabestani, "Photochemical Oxidation of Phenanthrene Sorbed on Silica Gel," *Environmental Science & Technology* 30 (1996): 1776–1780.
9. Y. Yang and F. Hildebrand, "Phenanthrene Degradation in Subcritical Water," *Analytica Chimica Acta* 555 (2006): 364–369.
10. E. Perraudin, H. Budzinski, and E. Villenave, "Identification and Quantification of Ozonation Products of Anthracene and Phenanthrene Adsorbed on Silica Particles," *Atmospheric Environment* 41 (2007): 6005–6017.
11. J. Lee and D. A. Lane, "Formation of Oxidized Products From the Reaction of Gaseous Phenanthrene With the OH Radical in a Reaction Chamber," *Atmospheric Environment* 44 (2010): 2469–2477.
12. D. E. Edwards, D. Y. Zubarev, W. A. Lester, and M. Frenklach, "Pathways to Soot Oxidation: Reaction of OH With Phenanthrene Radicals," *Journal of Physical Chemistry A* 118 (2014): 8606–8861.
13. N. Zhao, Q. Zhang, and W. Wang, "Atmospheric Oxidation of Phenanthrene Initiated by OH Radicals in the Presence of O₂ and NOx — A Theoretical Study," *Science of the Total Environment* 563/564 (2016): 1008–1015.
14. A. Maranzana, G. Ghigo, and G. Tonachini, "Anthracene and Phenanthrene Tropospheric Oxidation Promoted by the Nitrate Radical in the Gas-Phase. Theoretical Modelistic Study," *Atmospheric Environment* 167 (2017): 181–189.
15. V. S. Krasnoukhov, M. V. Zagidullin, I. P. Zavershinskiy, and A. M. Mebel, "Formation of Phenanthrene via Recombination of Indenyl and Cyclopentadienyl Radicals: A Theoretical Study Published as Part of the Journal of Physical Chemistry Virtual Special Issue 'Alexander Boldyrev Festschrift'," *Journal of Physical Chemistry A* 124 (2020): 9933–9941.
16. A. W. Fikri and A. Raj, "Growth of Polycyclic Aromatic Hydrocarbons by C₂H₂ Mediated by Five-Membered Rings: Acenaphthylene Conversion to Phenanthrene," *Combustion Science and Technology* 195 (2021): 619–645.
17. M. J. Frisch, G. W. Trucks, H. B. Schlegel, et al., Gaussian 16, Revision C.01 (Gaussian Inc., 2016).
18. Gaussian.com Expanding the limits of computational chemistry.
19. Y. Zhao and D. G. Truhlar, "The M06 Suite of Density Functionals for Main Group Thermo-Chemistry, Thermochemical Kinetics, Noncovalent Interactions, Excited States, and Transition Elements: Two New Functionals and Systematic Testing of Four M06-Class Functionals and 12 Other Functionals," *Theoretical Chemistry Accounts* 120 (2008): 215–241.
20. Y. Zhao and D. G. Truhlar, "Applications and Validations of the Minnesota Density Functionals," *Chemical Physics Letters* 502 (2011): 1–13.
21. A. Austin, G. Petersson, M. J. Frisch, J. F. Dobek, G. Scalmani, and K. Throssell, "A Density Functional With Spherical Atom Dispersion Terms," *Journal of Chemical Theory and Computation* 8 (2012): 4989–5007.
22. A. D. Becke, "Density-Functional Thermochemistry. III. The Role of Exact Exchange," *Journal of Chemical Physics* 98 (1993): 5648–5652.
23. C. Lee, W. Yang, and R. G. Parr, "Development of the Colic-Salvetti Correlation-Energy Formula Into a Functional of the Electron Density," *Physical Review B* 37 (1988): 785–789.
24. J. A. Montgomery, J. W. Ochterski, and G. A. Petersson, "A Complete Basis Set Model Chemistry. IV. An Improved Atomic Pair Natural Orbital Method," *Journal of Chemical Physics* 101 (1994): 5900–5909.

25. C. Sheng, "Elementary, Pressure Dependent Model for Combustion of C1, C2 and Nitrogen Containing Hydrocarbons: Operation of a Pilot Scale Incinerator and Model Comparison," *Dissertations* 518 (2002), <https://digitalcommons.njit.edu/dissertations/518>.
26. T. H. Lay, L. N. Krasnoperov, C. A. Venanzi, J. W. Bozzelli, and N. V. Shokhirev, "Ab Initio Study of α -chlorinated Ethyl Hydroperoxides $\text{CH}_3\text{CH}_2\text{OOH}$, $\text{CH}_3\text{CHClOOH}$, and $\text{CH}_3\text{CCl}_2\text{OOH}$: Conformational Analysis, Internal Rotation Barriers, Vibrational Frequencies, and Thermodynamic Properties," *Journal of Physical Chemistry* 100 (1996): 8240–8249.
27. C. Sheng, J. W. Bozzelli, A. M. Dean, and A. Y. Chang, "Detailed Kinetics and Thermochemistry of $\text{C}_2\text{H}_5 + \text{O}_2$: Reaction Kinetics of the Chemically Activated and Stabilized $\text{CH}_3\text{CH}_2\text{OO}\cdot$ Adduct," *Journal of Physical Chemistry A* 106 (2002): 7276–7293.
28. H. Wang and M. Frenklach, "Enthalpies of Formation of Benzenoid Aromatic Molecules and Radicals," *Journal of Physical Chemistry* 97 (1993): 3867–3874.
29. <https://webbook.nist.gov/chemistry>.
30. I. V. Tokmakov, G. S. Kim, V. V. Kislov, A. M. Mebel, and M. C. Lin, "The Reaction of Phenyl Radical With Molecular Oxygen: A G2M Study of the Potential Energy Surface," *Journal of Physical Chemistry A* 109 (2005): 6114–6127.
31. C. W. Zhou, V. V. Kislov, and A. M. Mebel, "Reaction Mechanism of Naphthyl Radicals With Molecular Oxygen. 1. Theoretical Study of the Potential Energy Surface," *Journal of Physical Chemistry A* 116 (2012): 1571–1585.
32. D. A. Bittker, "Detailed Mechanism for Oxidation of Benzene," *Combustion Science and Technology* 79 (1991): 49–72.

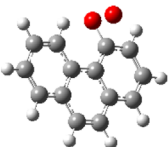
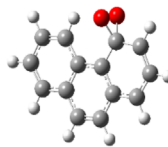
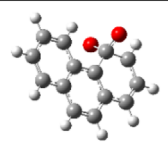
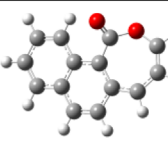
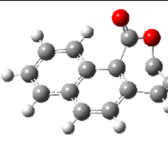
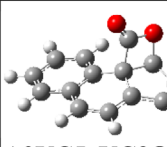
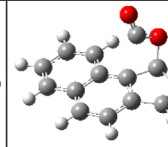
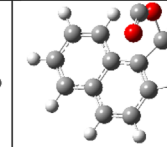
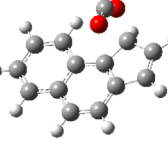
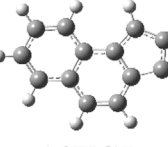
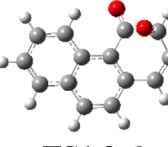
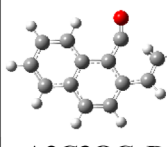
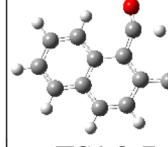
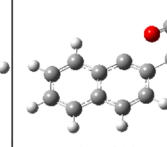
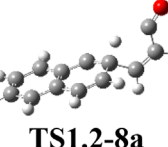
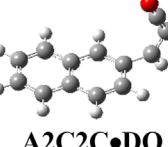
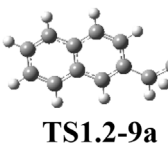
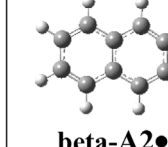
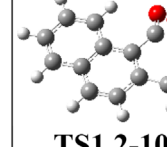
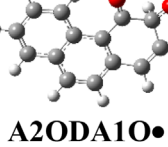
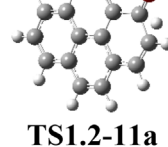
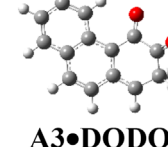
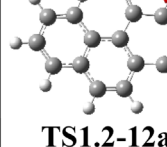
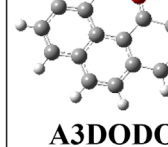
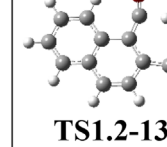
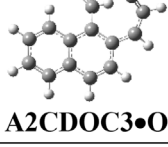
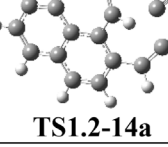
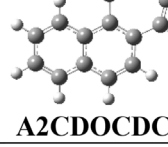
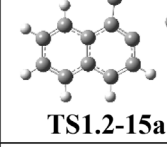
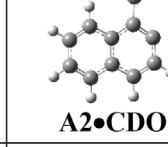
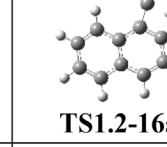
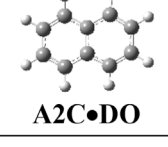
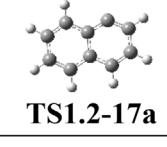
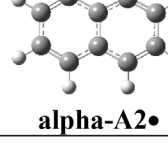
Appendix

TABLE A1 | Structures and nomenclature of intermediate species, transition states (TST), and products of Channels 1 to 3.

Channel 1.1: Formation and further reactions of $\text{A3}\cdot\text{YC2O2}$ Addition of the oxygen atom to the adjacent carbon atom					
					
TS1.1-1	A3•YC2O2	TS1.1-2	A3O•DO	TS1.1-3	A2YCDOOC•C2
					
TS1.1-4	A3DOYC2OC•	TS1.1-5	A2YC2OC•CDO	TS1.1-6	A2CC•CDOCD
					
TS1.1-7	A2•CDOCD	TS1.1-8	A2CDOC•DO	TS1.1-9	A2C•DO-alpha
					
TS1.1-10	alpha-A2•	TS1.1-11	A2YC5DO	TS1.1-12	A2YC5DOYC3•O
					
TS1.1-13	A2YC5•DOCD	TS1.1-14	A2YC5DO		

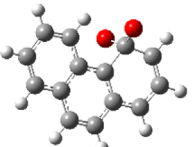
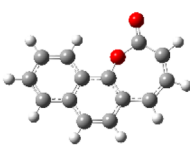
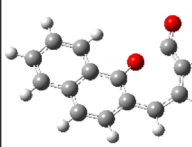
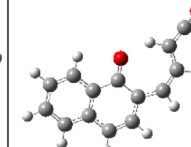
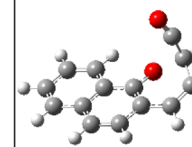
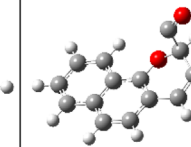
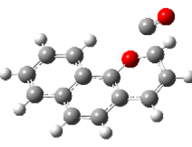
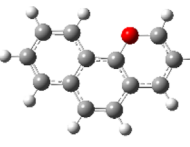
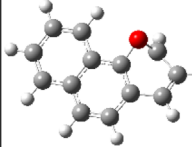
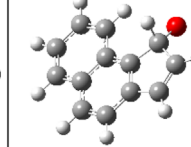
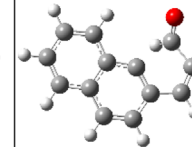
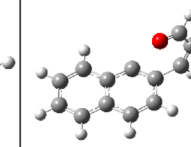
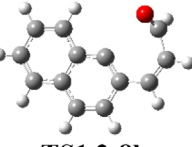
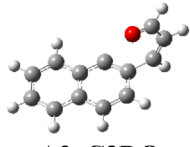
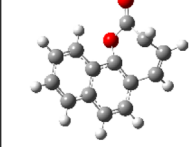
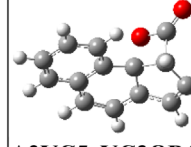
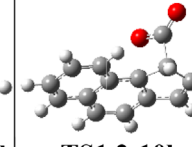
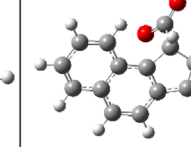
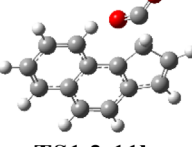
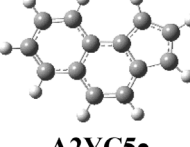
(Continues)

TABLE A1 | (Continued)

Channel 1.2: Formation and further reactions of A3•YCO2 Ipsso addition of the oxygen atom to the ring					
					
TS1.2-1	A2•YCO2				
Channel-1.2A					
					
TS1.2-2a	A2YCD0OC•CC	TS1.2-3a	A2YC5•YC3ODO	TS1.2-4a	A2YC5OC•DO
					
TS1.2-5a	A2YC5•	TS1.2-6a	A2C3OC•DO	TS1.2-7a	A2•C3DO
			CH ₂ =C=C=O		
TS1.2-8a	A2C2C•DO	TS1.2-9a	CH ₂ =C=C=O	beta-A2•	TS1.2-10a
					
A2ODA1O•	TS1.2-11a	A3•DODO	TS1.2-12a	A3DODO	TS1.2-13a
					
A2CDOC3•O	TS1.2-14a	A2CDOCDC•	TS1.2-15a	A2•CDO	TS1.2-16a
					
A2C•DO	TS1.2-17a	alpha-A2•			

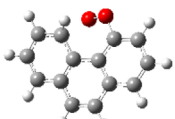
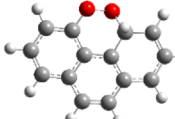
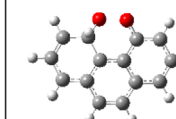
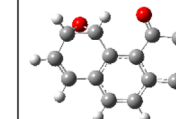
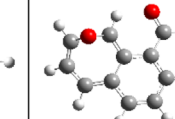
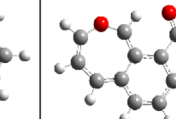
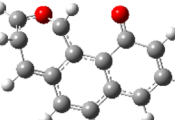
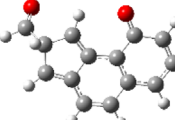
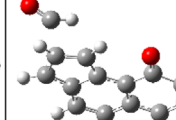
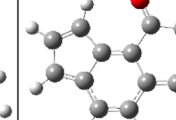
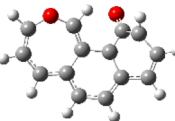
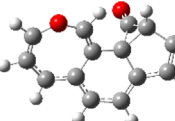
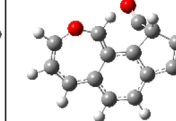
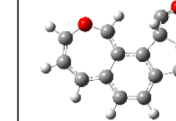
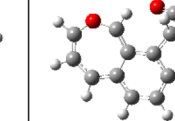
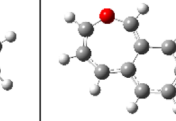
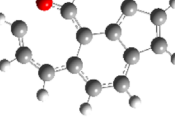
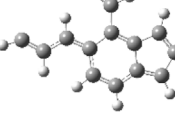
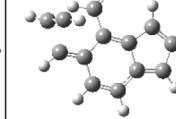
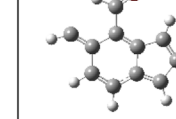
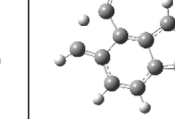
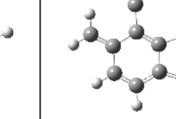
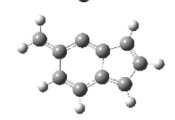
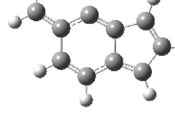
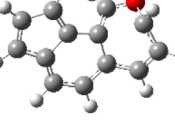
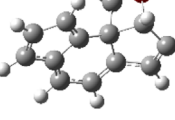
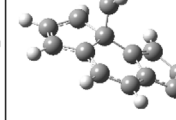
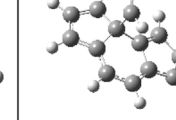
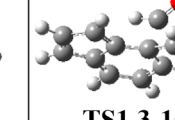
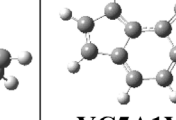
(Continues)

TABLE A1 | (Continued)

Channel-1.2B					
 TS1.2-2b	 A2YOCDOC•CC	 TS1.2-3b	 A2DOC4•O	 TS1.2-4b	 A2YC5OC•DO
 TS1.2-5b	 A2YC5•O	 TS1.2-6b	 A2YC5O•	 TS1.2-7b	 A2•C3DO
 TS1.2-8b	 A2•C3DO	 TS2-9b	 A2YC5•YC3ODOb	 TS1.2-10b	 A2YC5CO2•
 TS1.2-11b	 A2YC5•				

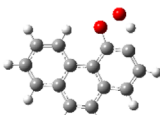
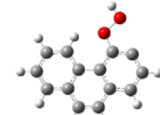
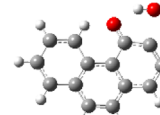
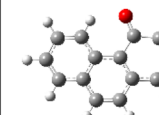
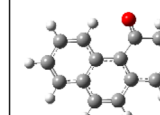
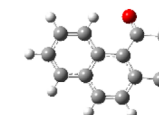
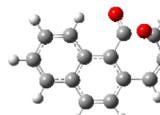
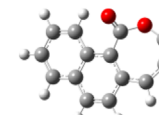
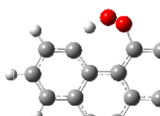
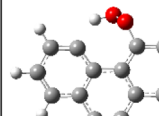
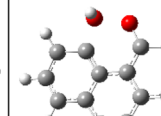
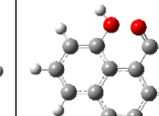
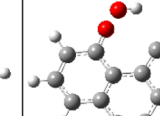
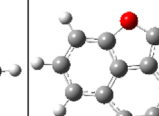
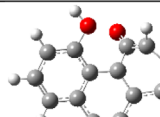
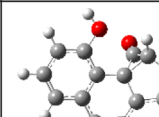
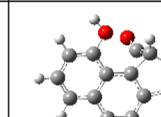
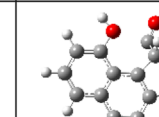
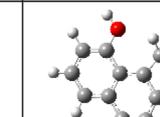
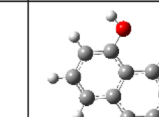
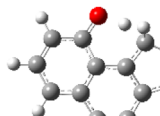
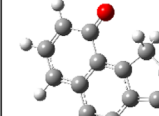
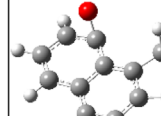
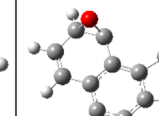
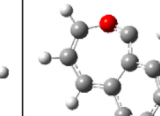
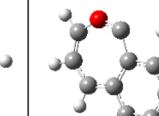
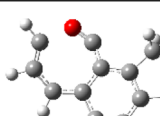
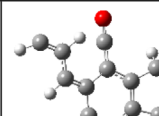
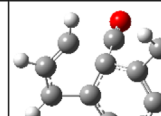
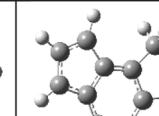
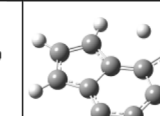
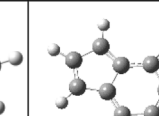
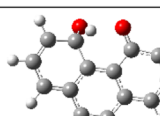
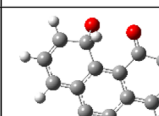
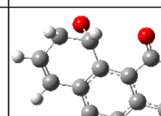
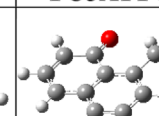
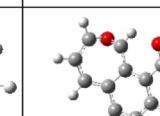
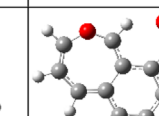
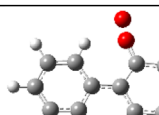
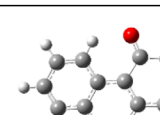
(Continues)

TABLE A1 | (Continued)

Channel 1.3: Formation and further reactions of A3•YC4O2 Addition of the oxygen atom to the opposite ring					
 TS1.3-1	 A3•YC4O2	 TS1.3-2	 A2•DOA1YC2O	 TS1.3-3	 A2DOYC6•O
 TS1.3-4	 A2DOYC5•CDO	 TS1.3-5	 A2DOYC5		
 TS1.3-6	 YC6OA1•YC5YC3DO	 TS1.3-7	 YC6OA1YC5C•DO	 TS1.3-8	 YC6OA1YC5•
 TS1.3-9	 YC5A1CDOC3•	 TS1.3-10	 YC5A1CDOC•	 TS1.3-11	 YC5A1DCC•DO
 TS1.3-12	 YC5A1•DC				
 TS1.3-13	 YC5A1YC5YC3•O	 TS1.3-14	 YC5A1YC5•CDO	 TS1.3-15	 YC5A1YC5


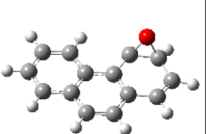
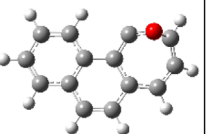
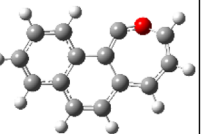
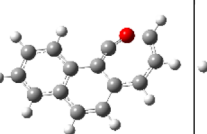
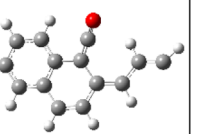
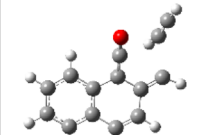
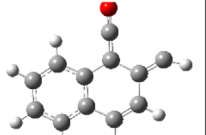
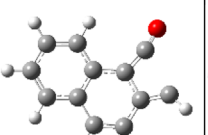
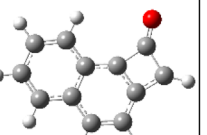
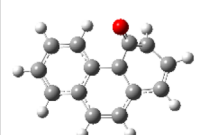
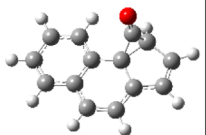
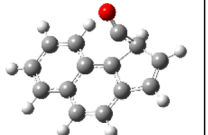
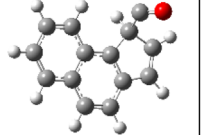
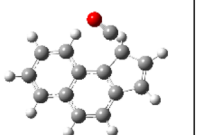
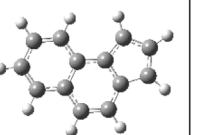
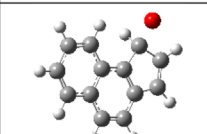
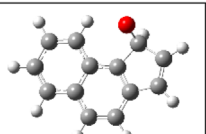
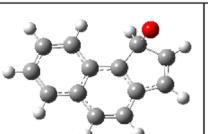
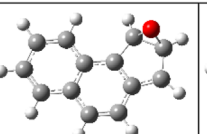
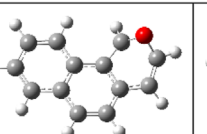
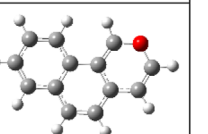
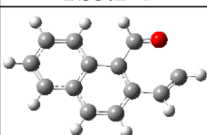
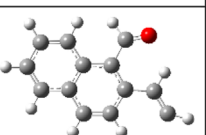
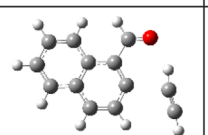
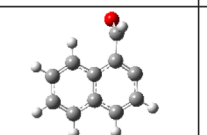
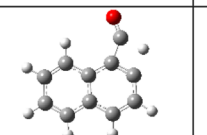
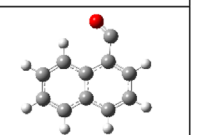
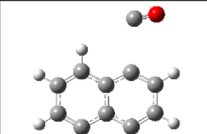
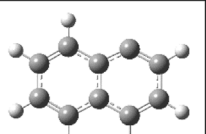
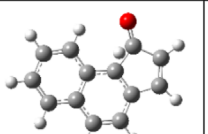
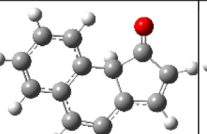
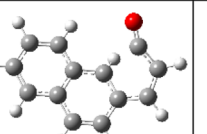
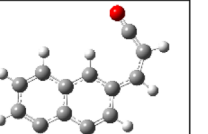
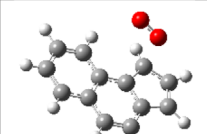
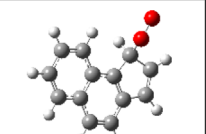
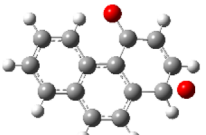
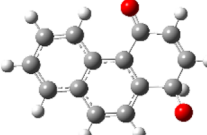
(Continues)

TABLE A1 | (Continued)

Channel 1.4: Formation and further reactions of A3•OOH					
Abstraction of hydrogen atom from the same ring					
 TS1.4a-1	 A3•OOH-a	 TS1.4a-2	 A2A1•OHDO	 TS1.4a-3	 A2A1O•DO
 TS1.4a-4	 A2YCD0OC•CC				
Abstraction of hydrogen atom from the opposite ring					
 TS1.4b-1	 A3•OOH-b	 TS1.4b-2	 A2OHA1•DO	 TS1.4b-3B	 A3YC4O
 TS1.4b-3	 A2OHYC5•YC3DO	 TS1.4b-4	 A2OHYC5C•DO	 TS1.4b-5	 A2OHYC5•
 TS1.4b-6	 ODA2•YC5	 TS1.4b-7	 YC5A2•YC2O	 TS1.4b-8	 YC5A1YC6•O
 TS1.4b-9	 YC5A1C3•DCDO	 TS1.4b-10	 YC5A1YC5•	 TS1.4b-11	 YC5A1YC5
 TS1.4b-12	 A2DOA1O•	 TS1.4b-13	 A2DOA1•YC2O	 TS1.4b-14	 A2DOYC6•O
Channel 2: O—O bond cleavage and formation of A3•DO					
 TS2			 A3•DO		

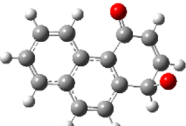
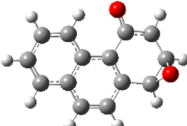
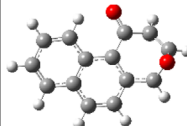
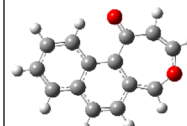
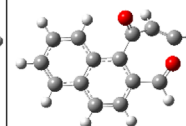
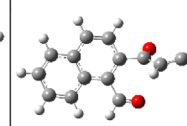
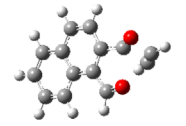
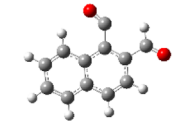
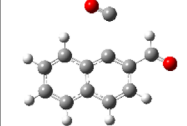
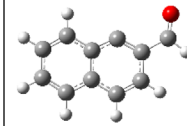
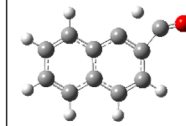
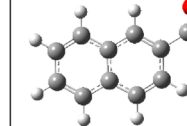
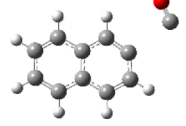
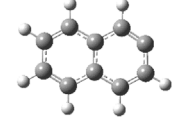
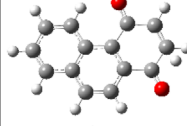
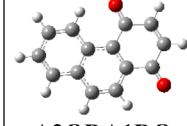
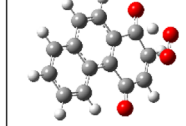
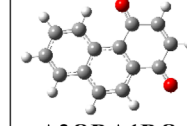
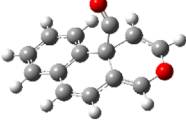
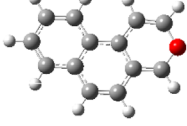
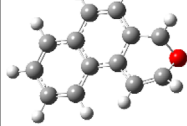
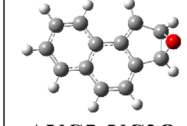
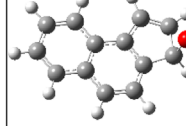
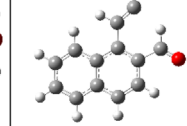
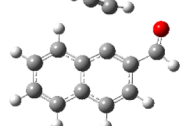
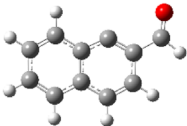
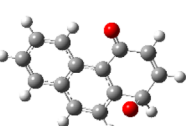
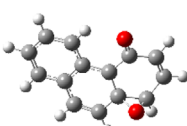
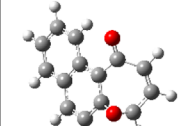
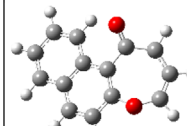
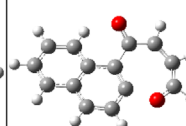
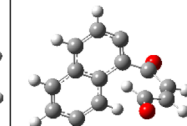
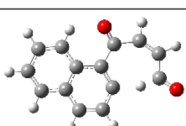
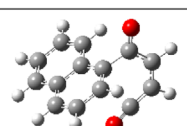
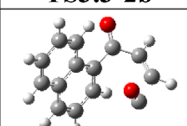
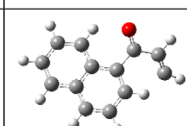
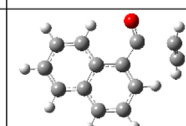
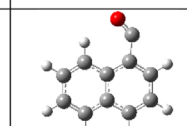
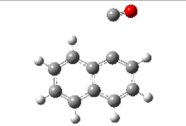
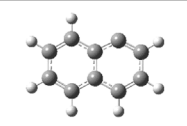
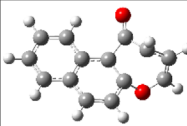
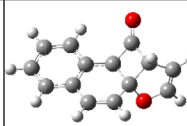
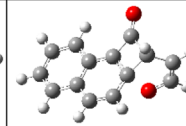
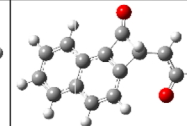
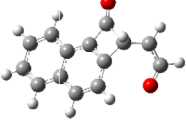
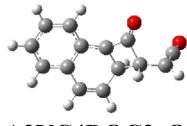
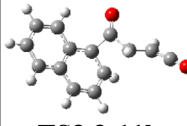
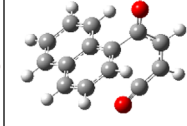
(Continues)

TABLE A1 | (Continued)

Channel 3.1: Further reactions of A3•DO					
					
TS3.1-1	A3•YC2O	TS3.1-2	A2YC•OC3	TS3.1-3	A2DCDOC3•
					
TS3.1-4	A2DCDOC•	TS3.1-5	A2YC4•DO		
Channel 3.2: Further reactions of A3•DO					
					
TS3.2-1	A2YC5•YC3DO	TS3.2-2	A2YC5C•DO	TS3.2-3	A2YC5•
Addition of an oxygen atom to A2YC5•					
					
TS3.2-4	A2YC5O•	TS3.2-5	A2YC5•YC2O	TS3.2-6	A2YC5•O
					
TS3.2-7	A2CDOC2•	TS3.2-8	A2•CDO	TS3.2-9	A2C•DO-alpha
					
TS3.2-10	alpha-A2•	TS3.2-11	A2•YC5DO	TS3.2-12	A2C2C•DO
Addition of O ₂ to A2YC5•					
					
TS3.2-4-O2	A2YC5O2•				
Formation of A3O•DO: Addition of an oxygen atom on C ₁₄ H ₉ O• = A3•DO + O					
					
TS3.3			A3O•DO		

(Continues)

TABLE A1 | (Continued)

Channel 3.3: Further reactions of A3O•DO					
					
TS3.3-1a	A3DOC•YC2O	TS3.3-2a	A2YCDOC2OC•	TS3.3-3a	A2CDOCDOC2•
					
TS3.3-4a	ODCA2C•DO	TS3.3-5a	A2•CDO-beta	TS3.3-6a	A2C•DO-beta
					
TS3.3-7a	beta-A2•	TS-H	A2ODA1DO	TS+O2	A2ODA1DO
					
TS3.3-8a	A2YC5•O	TS3.3-9a	AYC5•YC2O	TS3.3-10a	A2CDOC2•
					
TS3.3-11a	A2•CDO-beta				
					
TS3.3-1b	A3•DOYCY2O-b	TS3.3-2b	A2YCDOC2C•O	TS3.3-3b	A2•CDOC3DO
					
TS3.3-4b	A2CDOC3•DO	TS3.3-5b	A2CDOC2•	TS3.3-6b	A2C•DO-alpha
					
TS3.3-7b	A2•-alpha	TS3.3-8b	A2YC4OYC4•DO	TS3.3-9b	A2YC4•DOC2O
					
TS3.3-10b	A2YC4DOC2•O	TS3.3-11b	A2CDOC3•DO		